J. Fluid Mech. (2000), *vol.* 414, *pp.* 251–284. Printed in the United Kingdom

Acoustics of a two-dimensional compact jet impinging normally onto a flat plate

By CHIH-YU KUO AND ANN P. DOWLING

Cambridge University Engineering Department, Trumpington Street, Cambridge CB2 1PZ, UK

(Received 14 August 1998 and in revised form 2 February 2000)

Vortex sound is revisited for two-dimensional compact jets. The interactions between the flow and the rigid boundaries of the nozzle are included. Jets with steady upstream conditions and with imposed forcing are considered. A multipole expansion for the acoustic radiation is derived by the method of matched asymptotic expansion. The processes are carried out to higher order to obtain the quadrupole impingement sound in addition to the leading monopole. The emitted sound is found to be related to the vortical flow motion and the scattering of the incoming forcing from the nozzle interior. The flow motion is simulated incompressibly using a point vortex model. The discretization of the continuous vortex shedding is carefully treated to fulfil the Kutta condition and to eliminate spurious sound radiation. Numerical calculations are given for both free and forced jets. For small forcing, the leading monopole is weak and, under some circumstances, the quadrupole sound can be dominant.

1. Introduction

In this paper, sound generation by low-Mach-number impinging jets is revisited. The aim is to clarify the acoustic sources in the presence of the jet nozzle, especially the quadrupole of the impingement region and the effect of the interactions between the flow and the rigid nozzle boundaries.

For a high-speed jet blowing normally onto a flat plate, the impingement region is the major acoustic source. Periodic oscillations occur when the jet Mach number is higher than about 0.6, as investigated experimentally by Ho & Nosseir (1981) and Powell (1988). This is due to an acoustic feedback mechanism. Sutherland & Brown (1972) measure the acoustics of a slightly obliquely impinging jet (at 10° to the plate normal). They find the key feature of the quadrupole directivity when the self-sustained oscillations appear: the fundamental and its first harmonic have deep minima at about 48° and 50° to the normal to the plate. There is only a minor discrepancy from the theoretical angle of 54.7° for the minimum sound due to an axisymmetric quadrupole near a plane surface, predicted using an image argument by Powell (1991). Measurements of the directivity are more straightforward when the feedback mechanism leads to self-excited oscillations. Then the discrete tone has a significantly larger magnitude and better correlation between the signals at different locations than the other broadband noise sources. Its directivity pattern can therefore be readily determined.

When the jet speed is lower than the critical Mach number, the highly correlated periodic oscillation no longer exists. The jet motion is then of a turbulent nature, generating a broadband noise spectrum. However, theoretically, the turbulent quadrupole also has sound level minima at 45° even when the axisymmetric condition is relaxed, Powell (1991). More sophisticated experimental techniques are required to

extract this directivity. Shen & Meecham (1993) were able to verify the directivity of this quadrupole experimentally. They use a cross-correlation technique to analyse the signals sampled between pressure transducers on the plate and microphones around the jet. It is believed that this method enables them to filter out much of the sound other than that produced within the jet impingement region.

The difficulties of analysing the sound of turbulent impinging jets are mainly associated with the fact that the quadrupoles are inefficient sources of sound. In laboratories, the sound signals are easily masked by those from other source mechanisms. For example, the characteristic wavelength of sound for a slow jet is inversely proportional to the jet Mach number. When the Mach number is very small, this wavelength eventually becomes comparable to the spacing between the nozzle and the plate in a common experimental setup, such as the one of Shen & Meecham. Under these circumstances, ignoring the existence of the nozzle and the interactions between the interior and exterior flow field is questionable.

In an attempt to eliminate nozzle effects, experimentalists, in addition to exploiting the cross-correlation method discussed above, usually subtract their sound measurements for an impinging jet from those for a free jet from the same nozzle. The residual noise is defined to be the impingement noise. The sound pressure level of the impingement noise obeys the eighth-power law, e.g. Olsen, Miles & Dorsch (1972). This increase of the sound level with jet velocity is qualitatively demonstrated by Yates (1978). He models the impingement by a stagnation flow and concludes that the change of momentum provides the extra sources of sound.

However, the quadrupole source of impinging jets has more subtle properties and has not yet been solved satisfactorily. Howe (1979) considers the acoustic energy transmitted from the interior of a nozzle through a jet. He finds that, for a low-Mach-number jet, the radiation pattern is equivalent to a monopole and dipole combination to leading order. The axis of the dipole is parallel to the jet axis. Since the impinging jet is equivalent to the resultant of the jet itself and its image, the summation of the two opposite dipoles degenerates into quadrupoles associated with the jet exit. Moreover, the role of the additive monopoles is of particular interest and is ignored in the existing theories of impinging jets. These arguments also suggest that in order to solve the acoustic field properly, an analysis of high-order accuracy is required.

For simplicity, we investigate a two-dimensional impinging jet at this stage. This jet is assumed to be symmetric with respect to its axis. The subsonic jet not only generates sound which is radiated to the far field but also induces acoustic waves in the duct. Hence, we employ a matched asymptotic process to construct the leading-order solution. The theoretical derivation of an unforced jet is described in § 2 and a multipole expansion for the far-field acoustics is obtained. Section 2.7 briefly presents the extension to a forced jet, driven by acoustic waves propagating down the jet pipe. The multipole expansion of the acoustic far field shows that the sound source mechanism is divided into two major categories: the vortex sound of the shear layer motion and the scattering of any incoming sound propagating down the duct. Forcing also influences the shed vorticity through the Kutta condition at the nozzle exit and so modifies the vortex sound. The expansion is compared to Crow's (1970) and Möhring's (1978, 1979) theory of vortex sound.

We demonstrate theoretically how the vortex sound component can be expressed in terms of the motion of the shear layer. Various ways to describe the shear layer motion are available. We use a point vortex model to simulate the shear layer. A fourth-order integrator is applied to update the position of the vortices to the accuracy required for the vortex sound calculation. Application of the discrete vortex method

as sources of sound has been investigated by Knio, Collorec & Juve (1995) where the sound level from clusters of point vortices over a flat slippery boundary is calculated. This model enables us to describe not only the growth of the instabilities but also the nonlinear interactions, such as vortex pairing, in the impingement region. The numerical scheme is described in § 3.1.

In the calculation, the time step is set to a small finite value and, at each time step, a new vortex element is shed near the nozzle lip to fulfil the Kutta condition. During the shedding process, the new vortex is connected to the nozzle lip by a 'feeding sheet' which continuously feeds in vorticity. Peters & Hirschberg (1993) study the effect of the vortex shedding induced by an incident plane wave from the interior of a pipe. They note that there is, in general, a spurious dipole sound radiation due to the discretization. This dipole radiation is eliminated by correctly including the counterpart contribution from its image (Howe 1996). The amended shedding process is referred to as a 'sound-free Kutta condition'. We use it to model the continuous shedding of vorticity at the duct exit, as described in § 3.2. Numerical verifications of the hydraulic field are discussed in § 4.1. Finally, the simulated hydraulic flow is used in the acoustic analogy in § 4.2 and § 4.3 to determine the far-field sound. Two examples for both forced and unforced jets are given.

2. Far-field sound of compact impinging jets

Assuming that the flow is isentropic, we rewrite the equation of motion in the form of the exact acoustic analogy of Howe (1975), which uses stagnation enthalpy $B = \int \mathrm{d}p/\rho + u^2/2$ as the dependent variable:

$$\left(\frac{\mathrm{D}^*}{\mathrm{D}t^*}\left(\frac{1}{c^{*2}}\frac{\mathrm{D}^*}{\mathrm{D}t^*}\right) - \nabla^{*2}\right) B^* = \nabla^* \cdot (\boldsymbol{\omega}^* \times \boldsymbol{u}^*) - \frac{1}{c^{*2}}\frac{\mathrm{D}^*\boldsymbol{u}^*}{\mathrm{D}t^*} \cdot \frac{\partial^* \boldsymbol{u}^*}{\partial t^*}, \tag{2.1}$$

where we invoke the identity

$$\nabla^* B^* = -\partial^* \boldsymbol{u}^*/\partial t^* - \boldsymbol{\omega}^* \times \boldsymbol{u}^*. \tag{2.2}$$

The superscript * denotes dimensional physical quantities, and $\boldsymbol{u}$ and $\boldsymbol{\omega}$ are the flow velocity and vorticity.

The flow is divided into three regions, as sketched in figure 1. The inner region, Region I, is the hydraulic region where the flow is primarily incompressible. A variety of standard techniques can be used to evaluate the incompressible vortical flow. As an illustrative example, in § 3.1, we apply a point vortex model to simulate the flow motion. The jet exit velocity U_e and pipe width D are the characteristic velocity and length scale of the region. The non-dimensional inner variables are therefore

$$\tilde{B}_i(t, \boldsymbol{x}) = B^*(t, \boldsymbol{x})/U_e^2, \quad \boldsymbol{u} = \boldsymbol{u}^*/U_e, \quad \boldsymbol{\omega} = \boldsymbol{\omega}^* D/U_e, \quad \boldsymbol{x}_i = \boldsymbol{x}^*/D, \quad t = t^* U_e/D.$$

Equation (2.1) is non-dimensionalized to be

$$\left(M^2\frac{\mathrm{D}^2}{\mathrm{D}t^2} - \nabla_i^2\right)\widetilde{B}_i(t, \boldsymbol{x}) = \nabla_i \cdot (\boldsymbol{\omega} \times \boldsymbol{u}) + M^2\frac{\mathrm{D}\boldsymbol{u}}{\mathrm{D}t} \cdot \frac{\partial \boldsymbol{u}}{\partial t}, \tag{2.3}$$

where M is exit Mach number of the jet and is small throughout the analysis. After the normalization, the jet is driven by a steady uniform flow with unit velocity from infinity within the duct.

We also assume that the motion of the shear layer is the only acoustic source which generates sound waves. These waves both propagate through the outer wave

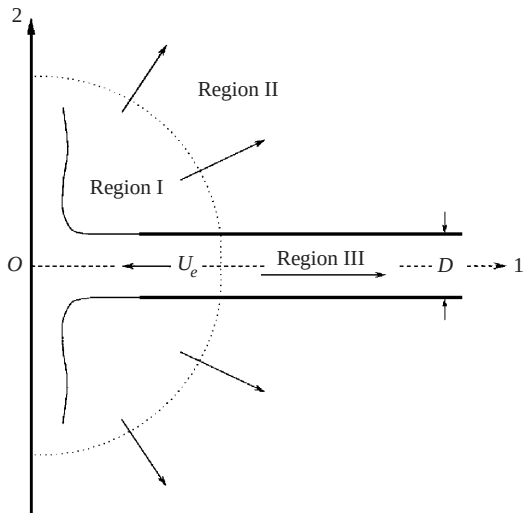

FIGURE 1. Schematic diagram of the flow regions: Region I, the inner region; Region II, the outer wave region and Region III, the duct wave region. The characteristic length scale is D for the inner region and D/M for the outer and duct regions. Mach number M is small.

region, Region II, and penetrate into the duct, Region III. For these propagating sound waves, we re-scale the outer wave variables to be

$$\tilde{B}_o(t,\boldsymbol{x}) = B^*(t,\boldsymbol{x})/U_e^2, \quad \boldsymbol{x}_o = M\boldsymbol{x}^*/D,$$

and the duct variables

$$\tilde{B}_D(t,\boldsymbol{x}) = B^*(t,\boldsymbol{x})/U_e^2, \quad \boldsymbol{x}_D = M\boldsymbol{x}^*/D.$$

Both regions have the same time scale as that of region I. Normalization of (2.1) using these non-dimensional variables gives the wave equation for the outer region

$$\left(\frac{\partial^2}{\partial t^2} - \nabla_o^2\right)\widetilde{B}_o(t,\boldsymbol{x}) = 0, \tag{2.4}$$

and the convective wave equation in the duct

$$\left(\left(\frac{\partial}{\partial t} - M\frac{\partial}{\partial x_D}\right)^2 - \frac{\partial^2}{\partial x_D^2}\right)\widetilde{B}_D(t,\boldsymbol{x}) = 0. \tag{2.5}$$

The method of matched asymptotic expansions is applied to match the solutions over the three regions.

The matching procedure is performed on the frequency domain. Taking Fourier transformation of (2.3), (2.4) and (2.5), one obtains

$$\nabla_i^2 B_i(\Omega,\boldsymbol{x}) = -\mathscr{F}\left\{\nabla_i\cdot(\boldsymbol{\omega}\times\boldsymbol{u}) + M^2\frac{\mathrm{D}\boldsymbol{u}}{\mathrm{D}t}\cdot\frac{\partial\boldsymbol{u}}{\partial t} - M^2\frac{\mathrm{D}^2}{\mathrm{D}t^2}\widetilde{B}_i\right\}, \tag{2.6}$$

for the inner region and

$$(\nabla_o^2 + \Omega^2)B_o(\Omega,\boldsymbol{x}) = 0, \qquad \left(\left(M\frac{\partial}{\partial x_D} + \mathrm{i}\Omega\right)^2 - \frac{\partial^2}{\partial x_D^2}\right)B_D(\Omega,\boldsymbol{x}) = 0, \tag{2.7}$$

for the outer wave region and the duct wave respectively. The operator $\mathscr{F}\{\}$ denotes

the transformation

$$B(\Omega) = \mathscr{F}\{\tilde{B}(t)\} = \int \tilde{B}(t) \exp(\mathrm{i}\Omega t)\mathrm{d}t,$$

where now the tilde marks the function B defined in the time domain. Velocity $\boldsymbol{u}$ and vorticity $\boldsymbol{\omega}$ remain functions of time.

To start the process, we try the first inner expansion

$$B_i(\Omega, \boldsymbol{x}) = B_i^{(0)}(\Omega, \boldsymbol{x}) + \text{h.o.t.},$$

where h.o.t. stands for higher-order terms. Substituting into (2.6), we obtain the governing equation for $B_i^{(0)}$

$$\nabla_i^2 B_i^{(0)}(\Omega, \boldsymbol{x}) = -\mathscr{F}\{\nabla_i \cdot (\boldsymbol{\omega} \times \boldsymbol{u})\}.$$

The solution after integration by parts once is

$$B_i^{(0)}(\Omega, \boldsymbol{x}) = \mathscr{F}\left\{\int (\boldsymbol{\omega} \times \boldsymbol{u}) \cdot \nabla_i G(\boldsymbol{x}_i, \boldsymbol{y}_i)\, \mathrm{d}\mathscr{V}_y\right\}, \tag{2.8}$$

where $G(\boldsymbol{x}_i, \boldsymbol{y}_i)$ is the Green function.

Solution (2.8) can be re-cast to a simpler form by applying Möhring's transformation Möhring (1978, 1979). For the two dimensional geometry, we can easily find a conjugate vector Green function $\boldsymbol{G}(\boldsymbol{x}_i, \boldsymbol{y}_i)$, satisfying $\nabla_i G(\boldsymbol{x}_i, \boldsymbol{y}_i) = \nabla_i \times \boldsymbol{G}(\boldsymbol{x}_i, \boldsymbol{y}_i)$. With this definition $\boldsymbol{G}(\boldsymbol{x}_i, \boldsymbol{y}_i)$ is undefined to within the addition of an arbitrary $\nabla f(\boldsymbol{x}_i, \boldsymbol{y}_i)$. Substitution into (2.8) yields

$$B_i^{(0)} = \mathscr{F}\left\{\int (\boldsymbol{\omega} \times \boldsymbol{u}) \cdot \nabla_i \times \boldsymbol{G}(\boldsymbol{x}_i, \boldsymbol{y}_i)\, \mathrm{d}\mathscr{V}_y\right\}$$

Integrating the right-hand side by parts, we have

$$B_i^{(0)} = \mathscr{F}\left\{\int \boldsymbol{G}(\boldsymbol{x}_i, \boldsymbol{y}_i) \cdot \nabla_i \times (\boldsymbol{\omega} \times \boldsymbol{u})\, \mathrm{d}\mathscr{V}_y\right\}.$$

Recalling the Helmholtz equation $\partial\boldsymbol{\omega}/\partial t = -\nabla_i \times (\boldsymbol{\omega} \times \boldsymbol{u})$ for inviscid and incompressible flow, the above expression becomes

$$B_i^{(0)}(\Omega, \boldsymbol{x}) = -\mathscr{F}\left\{\frac{\partial}{\partial t}\int \boldsymbol{\omega} \cdot \boldsymbol{G}(\boldsymbol{x}_i, \boldsymbol{y}_i)\, \mathrm{d}\mathscr{V}_y\right\}. \tag{2.9}$$

This procedure enables us to transform the quadratic form of vorticity and velocity, (2.8), into the time derivative of the linear superposition of vorticity and a vector Green function in the vortical flow region.

2.1. *The Green function and the far-field approximation of the hydraulic field*

Symmetrical perturbations are particularly observed to be the main source of the radiated sound (Powell 1988 and Neuwerth 1974), when a self-sustained feedback loop is established for high-speed impinging jets. From the intrinsic properties of free jets, Tam & Ahuja (1990) and Tam & Norum (1992) argued that the fundamental symmetric mode has a lower frequency band and is excited first as the jet velocity is raised to a critical Mach number. Therefore, we investigate a symmetric inner jet flow field for simplicity.

Under this simplification, Region I is reduced to a physical domain as shown in figure 2(*a*). The thin pipe wall is represented by the branch cut extending from z_e, the position of the exit, to infinity. A Schwartz–Christoffel transformation is

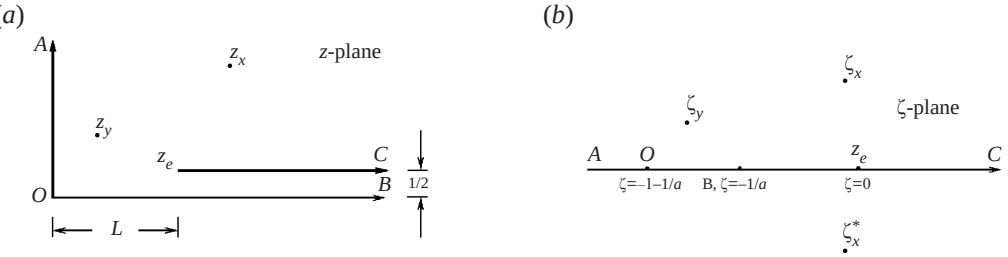

FIGURE 2. (*a*) The physical domain. (*b*) The conformal transformation domain. $z_x = x_1 + \mathrm{i}x_2$, $z_y = y_1 + \mathrm{i}y_2$ and ζ_x, ζ_y are the corresponding positions of z_x and z_y on the transformed plane.

applied to project the physical flow region z into the upper half-plane of the complex transformed variable ζ with the boundaries along the real axis, as shown in figure 2(*b*). The transformation (Kober 1952) is

$$\pi z = a\sqrt{\zeta + 1 + 1/a} + \tanh^{-1}\sqrt{\zeta + 1 + 1/a}, \tag{2.10}$$

where the width of the pipe has been normalized to unity and a is a real function of L, the distance from the pipe exit to the plate. This transformation maps the exit $z = z_e$ to the point $\zeta = 0$, and the stagnation point of the impingement, $z = 0$, to $\zeta = -1 - 1/a$. It is possible to remove the constraint of the symmetric impinging jet by employing a more sophisticated transformation and some extra algebraic details. One such transformation can also be found in Kober (1952). But no new physics is introduced by doing so.

The Green function $G(\boldsymbol{x}_i, \boldsymbol{y}_i)$ satisfies $\nabla_{iy}^2 G = \delta(\boldsymbol{y}_i - \boldsymbol{x}_i)$ and its normal derivatives vanish on axes and on the branch cut. Applying the conformal transformation, (2.10), G can be expressed as

$$G(\boldsymbol{x}_i, \boldsymbol{y}_i) = \frac{1}{2\pi}\mathrm{Re}\{\log(\zeta_y - \zeta_x) + \log(\zeta_y - \zeta_x^*)\}. \tag{2.11}$$

The ζ_x and ζ_y represent the corresponding positions of $\boldsymbol{x}$ and $\boldsymbol{y}$ on the transformed plane and the superscript $*$ denotes the complex conjugate. A suitable vector Green function, hence, can be written as

$$\boldsymbol{G}(\boldsymbol{x}_i, \boldsymbol{y}_i) = \frac{\boldsymbol{e}_3}{2\pi}\mathrm{Im}\{\log(\zeta_y - \zeta_x) + \log(\zeta_y - \zeta_x^*)\},$$

where $\boldsymbol{e}_3$ is the unit vector in the 3-direction.

The far-field approximation of (2.9) is found by letting $\zeta_x \to \infty$ in the vector Green function and the transformation (2.10), which leads to

$$B_i^{(0)} = \frac{a^2}{\pi^3}\frac{\cos(2\theta)}{r_i^2}\mathscr{F}\left\{\frac{\partial}{\partial t}\int \boldsymbol{\omega}\mathrm{Im}\{\zeta_y\}\,\mathrm{d}\mathscr{V}_y\right\} = -\frac{\mathrm{i}\Omega\cos(2\theta)}{r_i^2}\mathscr{Q}(\Omega), \tag{2.12}$$

where $r_i = (x_{i1}^2 + x_{i2}^2)^{1/2}$ in terms of inner variables and

$$\mathscr{Q}(\Omega) = \mathscr{F}\{\widetilde{\mathscr{Q}}(t)\} = \mathscr{F}\left\{\frac{a^2}{\pi^3}\int \boldsymbol{\omega}\mathrm{Im}\{\zeta_y\}\,\mathrm{d}\mathscr{V}_y\right\}. \tag{2.13}$$

Similarly we can find the approximation at the far end of the duct by letting $\zeta_x \to -1/a$, which gives

$$B_i^{(0)} = -\frac{1}{\pi}\mathscr{F}\left\{\frac{\partial}{\partial t}\int \boldsymbol{\omega}\mathrm{Im}\left\{\log\left(\zeta_y + \frac{1}{a}\right)\right\}\mathrm{d}\mathscr{V}_y\right\} = \frac{\mathrm{i}\Omega}{\pi}\mathscr{P}(\Omega), \tag{2.14}$$

and

$$\mathscr{P}(\Omega) = \mathscr{F}\{\widetilde{\mathscr{P}}(t)\} = \mathscr{F}\left\{\int \boldsymbol{\omega} \mathrm{Im}\left\{\log\left(\zeta_y + \frac{1}{a}\right)\right\} \mathrm{d}\mathscr{V}_y\right\}. \tag{2.15}$$

Equation (2.14) describes the 'back-reaction' within the duct of the exterior jet flow produced by the shear flow fluctuations. The independence of the upstream location expresses that, in the absence of compressibility, the shear layer source is incapable of inducing a net flux within the duct.

When the constraint of symmetry is removed, one can derive similar expressions to (2.12) and (2.14) for both the far-field and the duct approximation provided functions $\mathscr{P}(\Omega)$ and $\mathscr{Q}(\Omega)$ include the contributions from vortex elements in the region $\mathrm{Im}\,(z) < 0$.

2.2. *First-order matching with the duct wave*

The unsteadiness of the back-reaction induces sound waves. For simplicity, we assume that the duct is infinitely long so that there are no reflected acoustic waves. Therefore, the waves generated by the reactions are solely upstream propagating. Equation (2.14) suggests that the first expansion of the duct wave is

$$B_D = b_D \exp\left(\frac{\mathrm{i}\Omega x_D}{1-M}\right) + \text{h.o.t.}$$

The approximation when x_D is small is

$$B_D \simeq b_D(1 + \mathrm{i}\Omega x_D) = b_D + \mathrm{i}\Omega M x_i, \tag{2.16}$$

in terms of inner duct variable x_i, where we have $x_D = Mx_i$.

Equation (2.16) can be matched with (2.14) giving

$$b_D = \frac{\mathrm{i}\Omega}{\pi}\mathscr{P}(\Omega). \tag{2.17}$$

The expansion of (2.16) also suggests that the next order of the inner expansion is of magnitude $O(M)$. Moreover, as we see later, the outer wave equation (2.7) has its eigensolution expressed in terms of a Hankel function of zeroth order. Its logarithmic singularity is likely to introduce an additional term of $O(M \log M)$. Therefore, we assume the inner expansion is

$$B_i = B_i^{(0)} + M\, B_i^{(11)} + M \log M\, B_i^{(12)} + \text{h.o.t.} \tag{2.18}$$

On substituting into the governing equation of the inner region (2.6) we have equations $B_i^{(11)}$ and $B_i^{(12)}$, which are

$$\nabla_i^2 B_i^{(11)} = 0, \qquad \nabla_i^2 B_i^{(12)} = 0.$$

Their solution can be written down in the straightforward form

$$B_i^{(11)} = \frac{b_i^{(11,1)}}{2\pi}\mathrm{Re}\left\{\log\left(\zeta_x + \frac{1}{a}\right)\right\} + b_i^{(11,2)}, \tag{2.19}$$

and

$$B_i^{(12)} = \frac{b_i^{(12,1)}}{2\pi}\mathrm{Re}\left\{\log\left(\zeta_x + \frac{1}{a}\right)\right\} + b_i^{(12,2)}, \tag{2.20}$$

where the constants $b_i^{(11,1)}$, $b_i^{(11,2)}$, $b_i^{(12,1)}$ and $b_i^{(12,2)}$ are to be determined later.

Re-expressing the inner expansion (2.18) together with (2.19) and (2.20) the duct variable, we have

$$B_i \simeq \left\{ \frac{\mathrm{i}\Omega}{\pi}\mathscr{P}(\Omega) - \frac{b_i^{(11,1)}}{2}x_D \right\} + M\left\{ \frac{b_i^{(11,1)}}{2\pi}(a+\log 2) + b_i^{(11,2)} \right\} + M\log M\left\{ \frac{b_i^{(12,1)}}{2\pi}\left(a+\log 2 - \frac{\pi x_D}{M} \right) + b_i^{(12,2)} \right\}. \quad (2.21)$$

Comparison with (2.16) leads to

$$b_i^{(11,1)} = -2\mathrm{i}\Omega b_D = \frac{2\Omega^2}{\pi}\mathscr{P}(\Omega), \quad (2.22)$$

and

$$b_i^{(12,1)} = 0. \quad (2.23)$$

The lowest-order wave motion in the duct is order unity. This expansion also gives the next order of the duct wave expansion which, at least, contains $O(M)$ and $O(M\log M)$. The matching process for these higher-order terms is postponed until we finish the first-order matching with the wave region.

2.3. *First-order matching with the wave region*

To match with the wave region, we expand the far-field approximation of B_i in (2.18)–(2.20) in terms of outer variables,

$$B_i \simeq -M^2\frac{\mathrm{i}\Omega}{r_o^2}\cos(2\theta)\mathscr{Q}(\Omega) + M\left\{ \frac{1}{\pi}b_i^{(11,1)}\left(\log\frac{\pi}{a} + \log r_o \right) + b_i^{(11,2)} \right\} + M\log M\left(b_i^{(12,2)} - \frac{b_i^{(11,1)}}{\pi} \right) + O(M^3, \text{etc.}), \quad (2.24)$$

Hence, we can express the solution of (2.7) for the outer wave region by means of the multipole expansion

$$B_o = M\,b_o^{(1)}\mathrm{H}_0^{(1)}(\Omega r_o) + M\log M\,b_o^{(12)}\mathrm{H}_0^{(1)}(\Omega r_o) + M^2\{ b_o^{(21,1)}\mathrm{H}_0^{(1)}(\Omega r_o) + b_o^{(21,2)}\mathrm{H}_2^{(1)}(\Omega r_o)\cos(2\theta) \} + M^2\log M\,b_o^{(22)}\mathrm{H}_0^{(1)}(\Omega r_o), \quad (2.25)$$

where $\mathrm{H}_0^{(1)}(\Omega r_o)$ and $\mathrm{H}_2^{(1)}(\Omega r_o)$ are Hankel functions of order 0 and 2 of the first kind to satisfy the outgoing wave condition. The monopole term of $O(M^2)$ in (2.25) has to be retained because the higher-order expansion of the inner field usually results in it having non-zero strength which is comparable with the quadrupole in the wave region (Crighton, *et al.* 1992; Obermeier 1985). The term of $O(M^2\log M)$ also arises from the logarithmic singularity in the near field.

The near-field expansion of (2.25) is

$$B_o \simeq M\, b_o^{(1)} \left(\mathscr{A} + \frac{2\mathrm{i}}{\pi} \log r_o \right) + M \log M\, b_o^{(12)} \left(\mathscr{A} + \frac{2\mathrm{i}}{\pi} \log r_o \right)$$
$$+ M^2 \left\{ b_o^{(21,1)} \left(\mathscr{A} + \frac{2\mathrm{i}}{\pi} \log r_o \right) - \frac{4\mathrm{i}}{\pi(\Omega r_o)^2} b_o^{(21,2)} \cos(2\theta) \right\}$$
$$+ M^2 \log M\, b_o^{(22)} \left(\mathscr{A} + \frac{2\mathrm{i}}{\pi} \log r_o \right), \tag{2.26}$$

where $\mathscr{A} = 1 + (2\mathrm{i}/\pi)(\log \Omega/2 + \gamma_E)$, for short, and $\gamma_E \simeq 0.57$ is the Euler constant.

Matching (2.24) and (2.26) gives

$$\left.\begin{aligned} &b_o^{(1)} = -\tfrac{\mathrm{i}}{2} b_i^{(11,1)}, \quad b_o^{(12)} = 0, \quad b_o^{(21,2)} = \frac{\pi \Omega^3}{4} \mathscr{Q}(\Omega), \\ &b_i^{(11,2)} = \mathscr{A} b_o^{(1)} - \frac{b_i^{(11,1)}}{\pi} \log \frac{\pi}{a}, \quad b_i^{(12,2)} = \frac{1}{\pi} b_i^{(11,1)}. \end{aligned}\right\} \tag{2.27}$$

The constants $b_o^{(21,1)}$ and $b_o^{(22)}$ are not yet determined. Their values are derived from matching with the higher orders of the inner expansion and the duct wave.

The matching at this order shows that the interaction of the jet shear layer and the nozzle introduces a leading monopole of order M, as shown in Howe (1979). The quadrupole term is also revealed. It has a directivity $\cos(2\theta)$ which is imposed by the rigid boundary condition on the plate and the duct wall. The directivity pattern describes a minimum pressure at $\theta = 45^\circ$ in the first quadrant of the z-plane. This term, subjected to the geometric modification, corresponds to the quadrupole source of vortex sound in Crow (1970) and Möhring (1979) in an unbounded flow field.

2.4. *Second-order matching with the duct field*

Rewriting (2.26) in terms of inner variables, we have

$$B_o \simeq -\frac{4\mathrm{i}}{\pi(\Omega r_i)^2} b_o^{(21,2)} \cos(2\theta) + M\, b_o^{(1)} \left(\mathscr{A} + \frac{2\mathrm{i}}{\pi} \log r_i \right) + M \log M \frac{2\mathrm{i}}{\pi} b_o^{(1)}$$
$$+ M^2\, b_o^{(21,1)} \left(\mathscr{A} + \frac{2\mathrm{i}}{\pi} \log r_i \right) + M^2 \log M \left\{ \frac{2\mathrm{i}}{\pi} b_o^{(21,1)} + b_o^{(22)} \left(\mathscr{A} + \frac{2\mathrm{i}}{\pi} \log r_i \right) \right\}$$
$$+ M^2 \log^2 M \frac{2\mathrm{i}}{\pi} b_o^{(22)}. \tag{2.28}$$

This suggests that the second-order expansion of the inner field is

$$B_i = B_i^{(0)} + M B_i^{(11)} + M \log M B_i^{(12)}$$
$$+ M^2 B_i^{(21)} + M^2 \log M B_i^{(22)} + M^2 \log^2 M\, B_i^{(23)} + \text{h.o.t.} \tag{2.29}$$

Substituting (2.29) back into (2.6), we obtain the governing equations for each order

$$\nabla_i^2 B_i^{(21)} = \mathscr{F} \left\{ \frac{\mathrm{D}^2}{\mathrm{D}t^2} \tilde{B}_i^{(0)} - \frac{\mathrm{D}\boldsymbol{u}}{\mathrm{D}t} \cdot \frac{\partial \boldsymbol{u}}{\partial t} \right\},$$

and

$$\nabla_i^2 B_i^{(22)} = 0, \qquad \nabla_i^2 B_i^{(23)} = 0.$$

Their solutions are

$$B_i^{(21)} = \mathscr{F}\left\{\int\left(\frac{\mathrm{D}^2}{\mathrm{D}t^2}\tilde{B}_i^{(0)} - \frac{\mathrm{D}\boldsymbol{u}}{\mathrm{D}t}\cdot\frac{\partial \boldsymbol{u}}{\partial t}\right)G(\boldsymbol{x},\boldsymbol{y})\,\mathrm{d}\mathscr{V}_y\right\}$$
$$+\frac{1}{2\pi}b_i^{(21,1)}\mathrm{Re}\left\{\log\left(\zeta_x+\frac{1}{a}\right)\right\}+b_i^{(21,2)}, \quad (2.30)$$

with the aid of the Green function (2.11), and

$$\left.\begin{aligned} B_i^{(22)} &= \frac{b_i^{(22,1)}}{2\pi}\mathrm{Re}\left\{\log\left(\zeta_x+\frac{1}{a}\right)\right\}+b_i^{(22,2)},\\ B_i^{(23)} &= \frac{b_i^{(23,1)}}{2\pi}\mathrm{Re}\left\{\log\left(\zeta_x+\frac{1}{a}\right)\right\}+b_i^{(23,2)},\end{aligned}\right\} \quad (2.31)$$

respectively.

In the duct region, the expansion of B_i (2.29), in terms of the duct variable, is

$$B_i \simeq \left(\frac{\mathrm{i}\Omega}{\pi}\mathscr{P}(\Omega) - \tfrac{1}{2}b_i^{(11,1)}x_D\right) + M\left\{\frac{1}{2\pi}b_i^{(11,1)}(a+\log 2) + b_i^{(11,2)} - \tfrac{1}{2}b_i^{(21,1)}x_D\right\}$$
$$+M\log M\left\{b_i^{(12,2)} - \tfrac{1}{2}b_i^{(22,1)}x_D\right\} - M\log^2 M\,\tfrac{1}{2}b_i^{(23,1)}x_D + O(M^2\log M, \text{etc.}). \quad (2.32)$$

This expansion gives the next order of the duct wave as

$$B_D = b_D\exp(\mathrm{i}\Omega x_D) + M\,B_D^{(11)} + M\log M\,B_D^{(12)} + M\log^2 M\,B_D^{(13)} + \text{h.o.t.} \quad (2.33)$$

After substitution into the duct wave equation (2.7), we have the solutions

$$B_D^{(11)} = b_D^{(11)}\exp\left(\frac{\mathrm{i}\Omega x_D}{1-M}\right), \quad (2.34)$$

and

$$B_D^{(12)} = b_D^{(12)}\exp\left(\frac{\mathrm{i}\Omega x_D}{1-M}\right), \qquad B_D^{(13)} = b_D^{(13)}\exp\left(\frac{\mathrm{i}\Omega x_D}{1-M}\right). \quad (2.35)$$

The inner expansion of the duct wave, (2.33), bringing in (2.34) and (2.35), in terms of the duct variable then becomes

$$B_D = b_D(1+\mathrm{i}\Omega x_D) + M\{\mathrm{i}\Omega(b_D+b_D^{(11)})x_D + b_D^{(11)}\}$$
$$+M\log M\,b_D^{(12)}(1+\mathrm{i}\Omega x_D) + M\log^2 M\,b_D^{(13)}(1+\mathrm{i}\Omega x_D).$$

Matching the above equation with (2.32) gives

$$\left.\begin{aligned} &b_D^{(11)} = \frac{1}{2\pi}b_i^{(11,1)}(a+\log 2) + b_i^{(11,2)}, \quad b_D^{(12)} = b_i^{(12,2)},\\ &b_D^{(13)} = b_i^{(23,1)} = 0, \quad b_i^{(22,1)} = -2\mathrm{i}\Omega b_D^{(12)},\\ &b_i^{(21,1)} = -2\mathrm{i}\Omega(b_D+b_D^{(11)}).\end{aligned}\right\} \quad (2.36)$$

Information from the inner field also influences terms of orders M^2 and $M^2\log M$, etc. in the duct wave via (2.32). But we do not need to consider these higher-order terms. Finally, second-order matching with the wave region determines the rest of the unknown coefficients.

2.5. *Second-order matching with the wave region*

Incorporating the solutions for each magnitude order, such as (2.30) and (2.31), the far-field approximation of B_i in terms of inner variables is

$$B_i \simeq -\frac{\mathrm{i}\Omega}{r_i^2}\mathscr{Q}(\Omega)\cos(2\theta) + M\left(\frac{1}{\pi}b_i^{(11,1)}\left(\log\frac{\pi}{a}+\log r_i\right)+b_i^{(11,2)}\right)$$
$$+M\log M\, b_i^{(12,2)} + M^2\left\{\frac{1}{\pi}(2\mathscr{R}(\Omega)+b_i^{(21,1)})\left(\log\frac{\pi}{a}+\log r_i\right)+b_i^{(21,2)}\right\}$$
$$+M^2\log M\left\{\frac{1}{\pi}b_i^{(22,1)}\left(\log\frac{\pi}{a}+\log r_i\right)+b_i^{(22,2)}\right\}+M^2\log^2 M\, b_i^{(23,2)}. \quad (2.37)$$

The function

$$\mathscr{R}(\Omega) = \mathscr{F}\left\{\int\left(\frac{D^2}{Dt^2}B_i^{(0)} - \frac{D\boldsymbol{u}}{Dt}\cdot\frac{\partial \boldsymbol{u}}{\partial t}\right)\mathrm{d}\mathscr{V}_y\right\}. \quad (2.38)$$

is a term which results from the solution of (2.30) and represents compressibility effects from the first-order inner field. The evaluation of this function is described in Appendix A, § A.2 which gives $\mathscr{R}(\Omega) = -\Omega^2\mathscr{P}(\Omega)/\pi$ for inviscid flow.

Matching (2.37) and (2.28), we obtain the coefficients

$$\left.\begin{aligned} b_o^{(21,1)} &= -\frac{\mathrm{i}}{2}(2\mathscr{R}(\Omega)+b_i^{(21,1)}), \quad b_o^{(22)} = -\frac{\mathrm{i}}{2}b_i^{(22,1)},\\ b_i^{(21,2)} &= \mathscr{A}b_o^{(21,1)} - \frac{1}{\pi}(2\mathscr{R}(\Omega)+b_i^{(21,1)})\log\frac{\pi}{a},\\ b_i^{(22,2)} &= \frac{2\mathrm{i}}{\pi}b_o^{(21,1)} + \mathscr{A}b_o^{(22)} - \frac{1}{\pi}b_i^{(22,1)}\log\frac{\pi}{a},\\ b_i^{(23,2)} &= \frac{2\mathrm{i}}{\pi}b_o^{(22)}. \end{aligned}\right\} \quad (2.39)$$

This completes the matching process and gives the far field to order M^2. The coefficients are tabulated in (2.17), (2.23), (2.27), (2.36) and (2.39) for all the three regions and they are explicit functions of the incompressible vortical flow motion through $\mathscr{P}(\Omega)$, $\mathscr{Q}(\Omega)$, the frequency Ω and known constants.

2.6. *The sound waves in the outer wave region*

We are particularly interested in the outer wave region. From the matched asymptotic expansion, we obtain the acoustic field expressed by the multipole expression

$$B_o \simeq -M\frac{\mathrm{i}\Omega^2}{\pi}\mathscr{P}(\Omega)\mathrm{H}_0^{(1)}(\Omega r_o) + M^2\left\{\frac{\pi\Omega^3}{4}\mathscr{Q}(\Omega)\mathrm{H}_2^{(1)}(\Omega r_o) + b_o^{(21,1)}\mathrm{H}_0^{(1)}(\Omega r_o)\right\}$$
$$-M^2\log M\,\frac{2\Omega^3}{\pi^2}\mathscr{P}(\Omega)\mathrm{H}_0^{(1)}(\Omega r_o). \quad (2.40)$$

$\mathscr{P}(\Omega)$ and $\mathscr{Q}(\Omega)$ are functions of the incompressible vortical flow motion defined by (2.15) and (2.13):

$$\mathscr{P}(\Omega) = \mathscr{F}\left\{\int\boldsymbol{\omega}\mathrm{Im}\left\{\log\left(\zeta_y+\frac{1}{a}\right)\right\}\mathrm{d}\mathscr{V}_y\right\},$$

and

$$\mathscr{Q}(\Omega) = \mathscr{F}\left\{\frac{a^2}{\pi^3}\int \boldsymbol{\omega}\mathrm{Im}\,\{\zeta_y\}\,\mathrm{d}\mathscr{V}_y\right\}.$$

$\mathscr{P}(\Omega)$ is the integral of the product of the vorticity and the stream function of a hypothetical potential flow with a source at infinity in the duct. Its time derivative (2.14) is proportional to the hydraulic fluctuations at infinity in the duct induced by the exterior flow motion. $\mathscr{Q}(\Omega)$ has a similar form to $\mathscr{P}(\Omega)$ in which the hypothetical streamline is replaced by that of an irrotational uniform incoming flow as $y_2 \to \infty$.

The coefficient $b_o^{(21,1)}$ is found from (2.39) and relevant equations

$$b_o^{(21,1)} = -\mathrm{i}\mathscr{R}(\Omega) - \frac{\mathrm{i}\Omega^2}{\pi}\mathscr{P}(\Omega)\left(1 - \frac{\mathrm{i}\Omega}{\pi}(\mathscr{B} - \mathrm{i}\pi + 2\log\Omega)\right), \tag{2.41}$$

where $\mathscr{B} = a - \log 2 - 2\log(\pi/a) + 2\gamma_E$ is the constant that arises from the eigensolution of the wave region and the geometry detail.

It is, sometimes, more convenient to convert (2.40) back into the time domain when using a numerical calculation for the incompressible vortical flow in Region I. The algebraic detail is straightforward and is relegated to Appendix A. The equivalent expression in the time domain assuming the observer is far away from the source region is eventually found to be

$$\widetilde{B}_o(t,\boldsymbol{x}_o) \simeq M\widetilde{B}_o^{(1)}(t,\boldsymbol{x}_o) + M^2\log M\widetilde{B}_o^{(22)}(t,\boldsymbol{x}_o) + M^2\{\widetilde{B}_o^{(21,1)}(t,\boldsymbol{x}_o) + \widetilde{B}_o^{(21,2)}(t,\boldsymbol{x}_o)\cos(2\theta)\}, \tag{2.42}$$

where the monopoles $\widetilde{B}_o^{(1)}(t,\boldsymbol{x}_o)$, $\widetilde{B}_o^{(22)}(t,\boldsymbol{x}_o)$ and $\widetilde{B}_o^{(21,1)}(t,\boldsymbol{x}_o)$ are defined in (A 3), (A 4) and (A 14), respectively. $\widetilde{B}_o^{(21,2)}(t,\boldsymbol{x}_o)$ is the module of the quadrupole given by (A 16).

The leading-order term found in (2.42), $M\widetilde{B}_o^{(1)}(t,\boldsymbol{x}_o)$, is the response of the flow interaction with the exit of the duct. As expected, the quadrupole is of second order, and is accompanied by an induced monopole of the same order, often referred to as an 'isotropic quadrupole', and due to compressibility effects on the hydraulic motion in the inner field. $\widetilde{B}_o^{(22)}(t,\boldsymbol{x}_o)$ arises from the two-dimensional configuration of the flow field and explicitly from the logarithmic singularity of the Hankel function during the matching process. This expression also shows that when there is no forcing, the sound is generated due to the shear layer motion. The unsteadiness is introduced by the instability mechanism and the nonlinear interactions with the impingement.

2.7. *Forced jet*

It is also of interest to solve for the far-field acoustics subject to prescribed incident sound waves from infinity in the duct. To cope with the forcing, we replace the duct wave expansion by

$$B_D \simeq B_I\left(\exp\left(\frac{-\mathrm{i}\Omega x_D}{1+M}\right) + R\exp\left(\frac{\mathrm{i}\Omega x_D}{1-M}\right)\right) + Mb_D^{(11)}\exp\left(\frac{\mathrm{i}\Omega x_D}{1-M}\right) + M\log Mb_D^{(12)}\exp\left(\frac{\mathrm{i}\Omega x_D}{1-M}\right) + M\log^2 Mb_D^{(13)}\exp\left(\frac{\mathrm{i}\Omega x_D}{1-M}\right), \tag{2.43}$$

where B_I is the magnitude of the incident wave and is, in general, a function of frequency Ω. R is the reflection coefficient for the leading order. We here use the expansion of multiple scales for convenience and assume that the higher-order terms

only contain waves induced by the exterior flow motion and propagating upstream within the duct.

Both the outer wave region and the inner field have the same expansion as (2.25) and (2.29). We apply similar matching procedures as in the last section which leads to the reflection coefficient

$$R = \frac{\mathrm{i}\Omega}{\pi B_I}\mathscr{P}(\Omega) - 1, \tag{2.44}$$

and

$$b_i^{(11,1)} = -2\mathrm{i}\Omega B_I(R-1) = \frac{2\Omega^2}{\pi}\mathscr{P}(\Omega) + 4\mathrm{i}\Omega B_I. \tag{2.45}$$

The rest of the coefficients have the same dependence as expressed in (2.23), (2.27), (2.36) and (2.39). Through these expressions, the second term due to B_I in (2.45) causes responses at each order.

We can also obtain an equivalent expression in the time domain by using a similar inversion process to that described in the Appendix,

$$\widetilde{B}_{oF}(t,\boldsymbol{x}_o) = \widetilde{B}_o(t,\boldsymbol{x}_o) + M\left\{\frac{4}{\pi}\frac{\partial}{\partial t}\widehat{B}_I(t)\right\} + M^2\log M\left\{\frac{8}{\pi^2}\frac{\partial^2}{\partial t^2}\widehat{B}_I(t)\right\}$$
$$+M^2\frac{4}{\pi^2}\frac{\partial^2}{\partial t^2}\left\{\mathscr{B}\widehat{B}_I(t) + \sqrt{\frac{2}{r_o}}\widehat{H}_I(t)\right\}, \tag{2.46}$$

where $\widetilde{B}_o(t,\boldsymbol{x}_o)$ is found in (2.42) and

$$\widehat{B}_I(t) = \int_{-\infty}^{t-r_o} \mathrm{d}\tau\,((t-\tau)^2 - r_o^2)^{-1/2}\widetilde{B}_I(\tau),$$

$$\widehat{H}_I(t) = \int_{-\infty}^{t-r_o} \mathrm{d}\tau\,\frac{(\psi(1/2) - \log(t-\tau-r_o))}{(t-\tau-r_o)^{1/2}}\widetilde{B}_I(\tau).$$

The $\widetilde{B}_I(\tau)$ are the prescribed incident waves at the duct exit such that $\widetilde{B}_I(\tau) = \mathscr{F}^{-1}\{B_I(\Omega)\}$.

Equation (2.46) decomposes the acoustic source into two categories. One is the hydrodynamic motion of the jet expressed as $\widetilde{B}_o$. As we saw in § 2.1, this is the only sound source when the jet is unforced. The remaining terms are the direct scattering pattern from the incident waves through the duct exit region. Moreover, the forcing also affects the shed vorticity through the Kutta condition and, therefore, the resultant motion of the jet.

3. The model of the inner flow field

3.1. *The point vortex method*

We consider a two-dimensional subsonic jet which emerges from a straight pipe with a sharp exit and impinges normally onto a flat plate as sketched in figure 1. The flow is inviscid. Motion of the shear layer is described by the evolution of an array of point vortices. The velocity of an individual vortex in the system is mainly influenced by vortices in its vicinity as given by the Biot–Savart law. Compressibility effects which result in small modifications to the vortex element speed are neglected.

The vortical flow is simplified to a physical domain as shown in figure 3(*a*). Normal velocity vanishes on the axes and on the branch cut. The same Schwartz–Christoffel

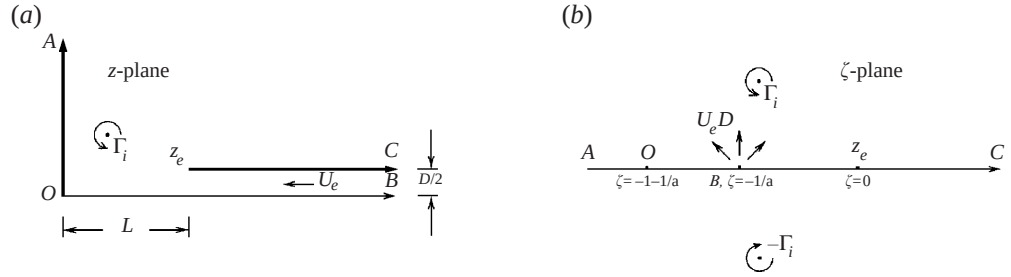

FIGURE 3. (*a*) The physical domain. (*b*) The conformal transformation domain.

transformation, (2.10), is again applied to project the physical flow region z into the upper half-plane of the complex transformed variable ζ with the boundaries along the real axis, as shown in figure 3(*b*). The jet is driven by a point source at $\zeta = -1/a$ with normalized unit volume flux at infinity in the duct. We can also simulate forced jets by adding small prescribed harmonic velocity perturbations onto the mean velocity at the source. A vortex is shed from the pipe exit at each calculation time step to satisfy the Kutta condition (see § 3.2). The point vortex is then convected with constant circulation after being introduced into the flow region. At any instant, we can find a complex potential in both the physical and transformed domains

$$\Psi(z) = \Phi(\zeta) = \frac{1}{2\pi} \log\left(\zeta + \frac{1}{a}\right) + \sum_i \frac{\Gamma_i}{2\pi \mathrm{i}} \log \frac{\zeta - \zeta_i}{\zeta - \zeta_i^*} \tag{3.1}$$

where Γ_i and ζ_i denote the circulation strength and the instantaneous position of the existing point vortices in the flow field. Superscript * denotes the complex conjugate. The image system of vortices is included to fulfil the boundary condition of zero normal velocity on the real axis of the computational domain.

The complex potential (3.1) gives the velocity at z,

$$u^*(z) = \frac{\mathrm{d}\Psi(z)}{\mathrm{d}z} = \frac{\mathrm{d}\Phi(\zeta)}{\mathrm{d}\zeta}\frac{\mathrm{d}\zeta}{\mathrm{d}z}. \tag{3.2}$$

The velocity of a vortex is, however, given by the local velocity induced by the rest of the vortices and the source, which is

$$u^*(z_i) = \lim_{z \to z_i} \frac{\mathrm{d}}{\mathrm{d}z}\left(\Psi(z) - \frac{\Gamma_i}{2\pi \mathrm{i}} \log(z - z_i)\right).$$

This can be rewritten as

$$u^*(z_i) = \lim_{z \to z_i} \frac{\mathrm{d}}{\mathrm{d}z}\left(\Phi_{\zeta_i}(\zeta) + \frac{\Gamma_i}{2\pi \mathrm{i}} \log(\zeta - \zeta_i) - \frac{\Gamma_i}{2\pi \mathrm{i}} \log(z - z_i)\right),$$

where the $\Phi_{\zeta_i}(\zeta)$ are the complex potentials excluding the contribution from the vortex of strength Γ_i at ζ_i corresponding to the physical position z_i. Applying the approximation

$$\zeta = \zeta_i + (z - z_i)\frac{\mathrm{d}\zeta}{\mathrm{d}z}\Big|_{z_i} + \tfrac{1}{2}(z - z_i)^2 \frac{\mathrm{d}^2\zeta}{\mathrm{d}z^2}\Big|_{z_i} + O((z - z_i)^3),$$

we obtain

$$u^*(z_i) = \Phi'_{\zeta_i}(\zeta)\Big|_{\zeta_i} \frac{\mathrm{d}\zeta}{\mathrm{d}z}\Big|_{z_i} + \frac{\Gamma_i}{4\pi \mathrm{i}} \frac{\mathrm{d}^2\zeta/\mathrm{d}z^2}{\mathrm{d}\zeta/\mathrm{d}z}\Big|_{z_i} \tag{3.3}$$

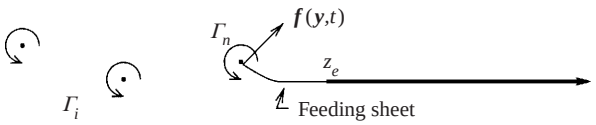

FIGURE 4. The imaginary vortical flow at an intermediate time step. Γ_n is the time-dependent circulation of the new vortex, Γ_i the constant circulation of the existing vortices and $\boldsymbol{f}(\boldsymbol{y},t)$ is the induced body force by Γ_n.

where $\Phi'_{\zeta_i}(\zeta)$ is the derivative of $\Phi_{\zeta_i}(\zeta)$ with respect to ζ. The second term on the right-hand side of (3.3) results from the transformation and is called the 'Routh's correction'.

Consequently, the convection velocity of the vortices in the computational plane is

$$\frac{\mathrm{d}\zeta_i}{\mathrm{d}t} = \frac{\mathrm{d}\zeta}{\mathrm{d}z}\bigg|_{z_i} \frac{\mathrm{d}z_i}{\mathrm{d}t} = u(z_i)\frac{\mathrm{d}\zeta}{\mathrm{d}z}\bigg|_{z_i}, \tag{3.4}$$

where $u(z_i)$ is given by (3.3). The derivatives $\mathrm{d}\zeta/\mathrm{d}z$ and $\mathrm{d}^2\zeta/\mathrm{d}z^2$ can be found from (2.10). Numerical calculations are carried out on the computational domain to solve (3.4) using a fourth-order Runge–Kutta algorithm, for example see Hildebrand (1956).

3.2. *Sound-free vortex shedding*

Flow separation occurs at the duct exit. For inviscid flow, vorticity is shed to ensure that the velocity at the exit is finite. This is commonly referred to as the Kutta condition. In point vortex calculations, a new vortex is shed at each time step. At beginning of a time step, a new vortex is specified at the position of the pipe exit. While we use the Runge–Kutta scheme to calculate the position of the other vortices at the intermediate steps, the new vortex is connected to the exit point by a 'feeding sheet' which allows vorticity to be continuously fed into the vortex during the time step, as sketched in figure 4. Following Howe (1996), the circulation of the feeding sheet is assumed to be negligible compared to that of the vortex.

The Kutta condition determines the circulation of the new vortex as a function of its position, but more detailed fluid dynamic analysis is required to determine the position of the vortex. The widely used Brown & Michael (1954) equation is derived by requiring that the shedding process does not generate forces on the flow field. Disselhorst & van Wijngaarden (1980) locate the new vortex at the centre of gravity of a small continuous sheet vortex segment shed during a time step. Comparison of various methods is made by Peters (1993). He finds that dipole sound radiation usually accompanies the discretized shedding process. This is because when the circulation of the new vortex is time dependent, it induces forces on both the feeding sheet and on the new vortex, as denoted by $\boldsymbol{f}(\boldsymbol{y},t)$ in figure 4, and generates the spurious dipole sound (see § 2.3 in Peters & Hirschberg 1993). Howe (1996) points out that this is due to an unbalanced surface force and derives an amended equation of motion for the new vortex by correctly including the surface contribution. In this section, we describe the incorporation of this shedding mechanism to eliminate the spurious sound from the discretization.

The Kutta condition states that the velocity (3.2) at the separation point is finite. Since the transformation $\mathrm{d}\zeta/\mathrm{d}z$ is singular at the exit, the circulation of the vortex must satisfy

$$\lim_{\zeta\to 0}\frac{\mathrm{d}}{\mathrm{d}\zeta}\left(\Phi(\zeta) + \frac{\Gamma_n}{2\pi\mathrm{i}}\log\frac{\zeta-\zeta_n}{\zeta-\zeta_n^*}\right) = 0,$$

where ζ_n is the position of the new vortex and $\Phi(\zeta)$ is the potential at ζ due to the existing vortices. This gives the circulation as a function of ζ_n

$$\Gamma_n = \frac{2\pi i \zeta_n \zeta_n^*}{\zeta_n^* - \zeta_n} \Phi'(0). \tag{3.5}$$

Because the circulation strength of the new vortex is time dependent, an unsteady force $\boldsymbol{f}(\boldsymbol{y}, t)$ is induced and acts on the vortex and the feeding sheet. This additional force arises solely due to the attempt to discretize the process of continuous vortex shedding. To ensure that it does not generate sound, Howe (1996) shows that the equation of motion for the new vortex should be

$$\frac{\mathrm{d}\boldsymbol{y}_n}{\mathrm{d}t} \cdot \nabla \Theta_j + \frac{\Theta_j}{\Gamma_n} \frac{\mathrm{d}\Gamma_n}{\mathrm{d}t} = \boldsymbol{u}(\boldsymbol{y}_n) \cdot \nabla \Theta_j \quad (j = 1, 2), \tag{3.6}$$

which is given in the Cartesian coordinates. $\Theta_j(\boldsymbol{y})$ is a hypothetical stream function which is zero on the boundaries and leads to a unit uniform speed in the j-direction as $|\boldsymbol{y}| \to \infty$. $\boldsymbol{y}_n$ and Γ_n denote the position and time-dependent circulation of the new vortex and $\boldsymbol{u}(\boldsymbol{y}_n)$ is the velocity induced at $\boldsymbol{y}_n$ by the rest of the vortices. A straightforward verification that the condition in (3.6) leads to silent vortex shedding is given in Kuo (1998).

The vortex shedding occurs near the pipe exit in this model; therefore, Θ_j is approximated by the stream functions of vortices near a semi-infinite plane extending from z_e to infinity parallel to the y_1-axis. For the case $j = 1$, the stream function with unit velocity in the y_1-direction is $\Theta_1 = \mathrm{Im}\{z - z_e\}$ and (3.6) provides the velocity component $\mathrm{d}\boldsymbol{y}_n/\mathrm{d}t$ normal to the half-plane. For $j = 2$, Θ_2 is defined by the limiting value as $b \to \infty$ of the stream function for a plate extending from z_e to $z_e + 2b$, namely,

$$\Theta_2 = \lim_{b \to \infty} \mathrm{Im}\{-\mathrm{i}((z - z_e)(z - z_e - 2b))^{1/2}\} \simeq \mathrm{Im}\{\sqrt{2b}(z - z_e)^{1/2}\}.$$

The length $2b$ does not appear in the equation of motion because (3.6) is homogeneous in Θ_j. Straightforward algebra combines the two cases into a single equation in complex-variable notation:

$$\frac{\mathrm{d}z_n}{\mathrm{d}t} + \frac{(z_n - z_e) - |z_n - z_e|}{\Gamma_n} \frac{\mathrm{d}\Gamma_n}{\mathrm{d}t} = u(z_n), \tag{3.7}$$

where $z = y_1 + \mathrm{i}y_2$ and $u(z_n)$ is the induced velocity, (3.3), on the z-plane. This is the equation of motion for the new vortex. It shows that the vortex velocity is equal to the induced velocity only when the circulation Γ_n is constant.

Equation (3.7) can be re-expressed in terms of the transformed variable

$$2\zeta_n \frac{\mathrm{d}\zeta_n}{\mathrm{d}t} + (\zeta_n^2 - |\zeta_n|^2) \frac{1}{\Gamma_n} \frac{\mathrm{d}\Gamma_n}{\mathrm{d}t} = \frac{4\pi}{Da^2}(1 + 1/a)^{1/2} u(z_n), \tag{3.8}$$

where we have assumed that the position of the new vortex is close to the exit z_e and applied the approximate form of (2.10)

$$\zeta_n^2 = \frac{4\pi}{Da^2}(1 + 1/a)^{1/2}(z_n - z_e).$$

Differentiating the circulation (3.5) with respect to time, we have

$$\frac{1}{\Gamma_n} \frac{\mathrm{d}\Gamma_n}{\mathrm{d}t} = \frac{1}{\zeta_n^* - \zeta_n} \left(\frac{\zeta_n^*}{\zeta_n} \frac{\mathrm{d}\zeta_n}{\mathrm{d}t} - \frac{\zeta_n}{\zeta_n^*} \frac{\mathrm{d}\zeta_n^*}{\mathrm{d}t} \right) + \frac{1}{\Phi'(0)} \frac{\mathrm{d}\Phi'(0)}{\mathrm{d}t}.$$

Substituting the above expression into (3.8), we find a more convenient form for the velocity of the new vortex on the computational plane

$$2\zeta_n \frac{\mathrm{d}\zeta_n}{\mathrm{d}t} - \zeta_n \left(\frac{\zeta_n^*}{\zeta_n} \frac{\mathrm{d}\zeta_n}{\mathrm{d}t} - \frac{\zeta_n}{\zeta_n^*} \frac{\mathrm{d}\zeta_n^*}{\mathrm{d}t} \right) = \mathscr{U}(\zeta_n; \zeta_j), \tag{3.9}$$

where

$$\mathscr{U}(\zeta_n; \zeta_j) = \frac{4\pi}{Da^2}(1 + 1/a)^{1/2} u(z_n) - \frac{\zeta_n^2 - |\zeta_n|^2}{\Phi'(0)} \frac{\mathrm{d}\Phi'(0)}{\mathrm{d}t}.$$

Equations (3.5) and (3.9) can be used to determine the evolution of the new vortex through its first time step.

We note that $\Phi'(0)$ is zero at the beginning of the time step because the Kutta condition was satisfied after the previous vortex was incorporated into the flow at the end of the previous time step. The right-hand side of (3.9) is therefore indefinite at that moment and we need to evaluate the path and velocity of the new vortex more carefully. The detailed algebra is described in Appendix B.

In the Runge–Kutta numerical scheme, we introduce a new vortex at $\zeta_n = 0$ at each time step and apply the similarity equation (B 1) of Appendix B to calculate its departing velocity. Then, (3.3) and (3.1) are used to update the subsequent vortex displacements at the intermediate steps of the scheme. A smaller time step is used if any of the vortices collides with any other or tries to cross the solid boundaries. This check is important to avoid any numerical singularities when finding the acoustic field from the vortex motion. This procedure is repeated until the prescribed terminal time. The computation time for each time step increases as the square of the number of vortices in the flow field and, in practice, this limits the calculation period. Examples of calculations of the inner hydraulic field are given in § 4.1.

4. Numerical results

We use the point vortex model to simulate the inner hydraulic flow field and hence to describe the sources of sound. In § 4.1, we discuss the simulation results of the inner flow for both forced and unforced jets. The nozzle to plate distance is set at $L = 3.0$ and the time step is $\delta t = 0.133$. A new vortex is shed at each time step. This calculated inner flow is subsequently used to find the far-field acoustic signals for the unforced and forced jets in §§ 4.2 and 4.3 respectively.

4.1. *Hydrodynamic flow field*

In this section, we briefly describe the hydraulic field of the impinging jet. As seen in § 3.1, the jet is driven by a point source on the transformation plane. If the jet is unforced, the strength of the source is a constant which is unity after normalization. We also consider a harmonically forced jet by specifying the strength of the source to be $1 + \tilde{u}' \cos \Omega_0 t$. As an example, the amplitude of the forcing relative to the mean jet velocity at the exit is $\tilde{u}' = 0.014$. The frequency is $\Omega_0 = 2.20$ which is believed to be in range of the preferred frequency for the jet excitation (Crow & Champagne 1971).

At the initial stage of the numerical simulation, the jet suddenly starts from rest. The vortex element shed from the pipe exit at each time step rolls up to form a starting vortex. The temporal development of the vortex is shown in figure 5(*a–d*). As the circulation of the jet increases, the vortex is convected towards the impingement plate. There are instabilities occurring between the rolled-up part of the vortex and the straight line vortex element array near the duct exit. This is due to a similar

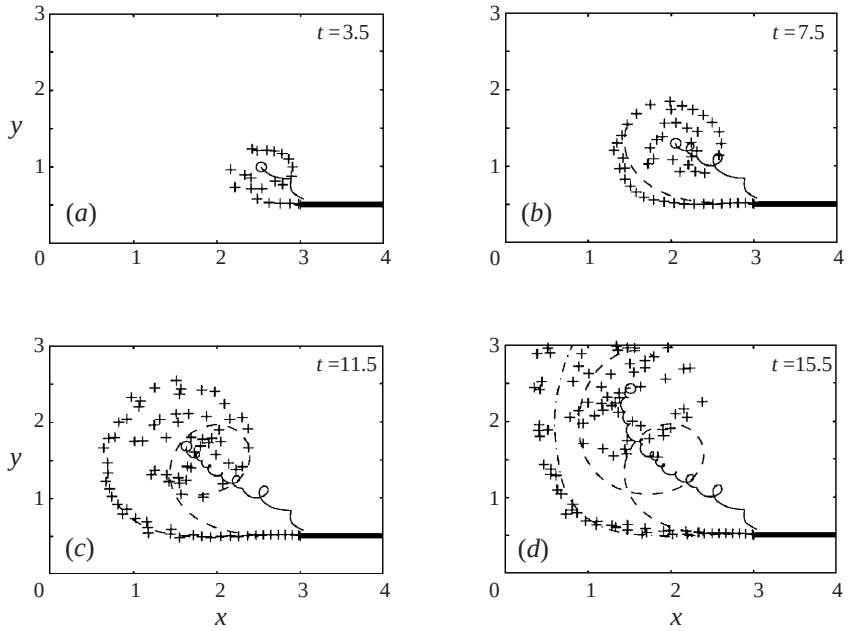

FIGURE 5. The development of the starting vortex: +, vortex elements; ○, the first vortex element. ——, — — —, and — · —, traces of the vortex elements shed at $t = 0, 4.53$ and 8.53 respectively.

mechanism to the Kelvin–Helmholtz instability. The growing disturbances as the elements roll into the vortex destroy the spiral structure of the starting vortex. These phenomena are also seen in studies of the roll-up of a finite vortex sheet, see Moore (1974), Baker (1979) and Krasny (1987). The traces of three selected vortex elements all show the characteristic of cyclic motion around a moving centre. The time scale of the starting vortex and jet development is of order D/U.

The circulation of the new vortex element shed at each time step is plotted as a function of time in figure 6. If the jet is unforced, the circulation settles to a constant with negligible fluctuations after a transient period as shown in figure 6(*a*). On the other hand, the forced case, figure 6(*b*), shows a harmonic variation in circulation with the same frequency as the forcing. Despite this, the difference between the characteristics of the starting vortex for the two cases is negligible.

The influence of the starting vortex on the impingement region fades out as it moves away from this region and an impinging jet emerges after a sufficiently long time from the start. A typical distribution of vortex elements is shown in figure 7. The instabilities of the vortex array grow as the vortex elements move downstream and result in distinguishable small eddies which consist of a group of elements after a distance of roughly half the jet pipe width downstream of the exit. Though it is a two-dimensional configuration, this agrees with the axisymmetrical jet results (Acton 1980). The eddies are significantly increased in size when they are near the impingement plane and in the wall jet region. The traces of four selected vortex elements show that their motion is confined in the shear layer of the impinging jet. Just as they depart from the pipe exit, these elements are initially convected within a well-defined shear layer. After a convected distance of half the pipe width or so, the growing instabilities separate the traces. The developing cyclic motion triggered by

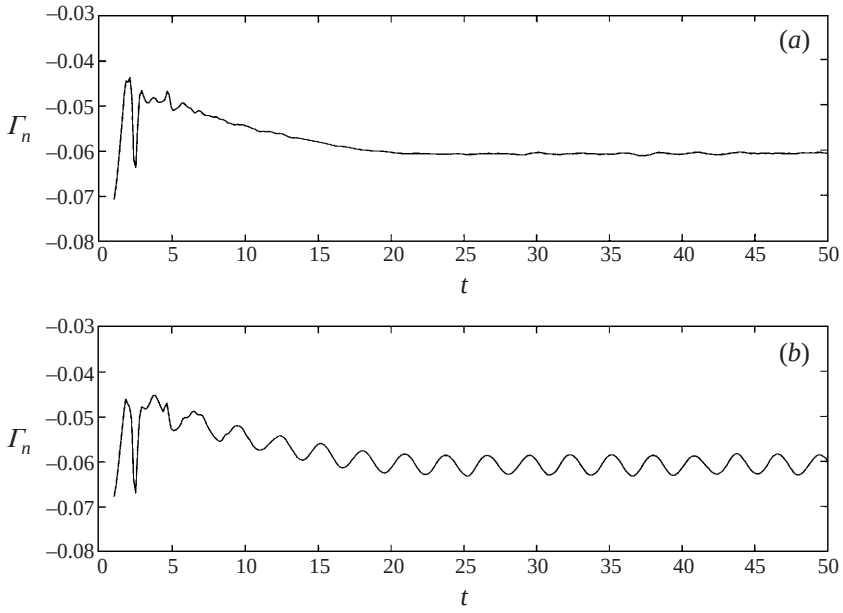

FIGURE 6. The circulation of the new vortex element as a function of time: (*a*) unforced case; (*b*) forced case.

the instabilities indicates that the elements are incorporated into eddies so that they not only move with the mean flow, but also rotate in these eddies.

Merging of successive eddies in the impingement region is also found. A sequence showing the merging process is given in figure 8(*a–f*). The familiar threading mechanism of vortex arrays is seen in the sequence of figure 8(*a–c*) where eddy A, referring to the caption of the figure, changes its direction of motion as it approaches the plane and its induced velocity accelerates eddy B towards the plane. Then eddy B, acquiring a faster velocity from its image, catches up and passes A. The two vortices combine into a co-rotating pair which eventually coalesces and they lose their separate identities, figure 8(*d–f*). This is commonly referred to as 'vortex pairing'. A similar mechanism also takes place in the wall jet region.

Vortex pairing is associated with subharmonic excitations. This can be demonstrated by comparing the spectral density functions of the hydraulic fluctuations at different streamwise observation points. Figure 9 shows the power spectral density of the time history of stagnation enthalpy at points inside the unforced incident and wall jet. The definition of the stagnation enthalpy in this point vortex model is $B(\boldsymbol{x}, t) = -\partial\phi(\boldsymbol{x}, t)/\partial t$ where $\phi(\boldsymbol{x}, t)$ is given by the real part of (3.1). Figure 9(*a*) basically represents small broadband fluctuations at a point on the pipe exit plane. The instability mechanism occurring as the vortex elements convect towards the impingement plane significantly amplifies the fluctuations, for example the fluctuations at the point near to the impingement region, figure 9(*b*). In this figure, a recognizable frequency band of noise, which is roughly between 1 and 5, is particularly excited and characterizes the unsteady flow field. After the impingement, the broadband noise tends to shift to a lower frequency range, as in figure 9(*c*). The modes with frequency around 0.5 after the second subharmonic excitation dominate the fluctuations beyond some distance away from the impingement, figure 9(*d*). Self-sustained oscillations for the unforced jet are not found. This is in contrast to a broad class of shear flows

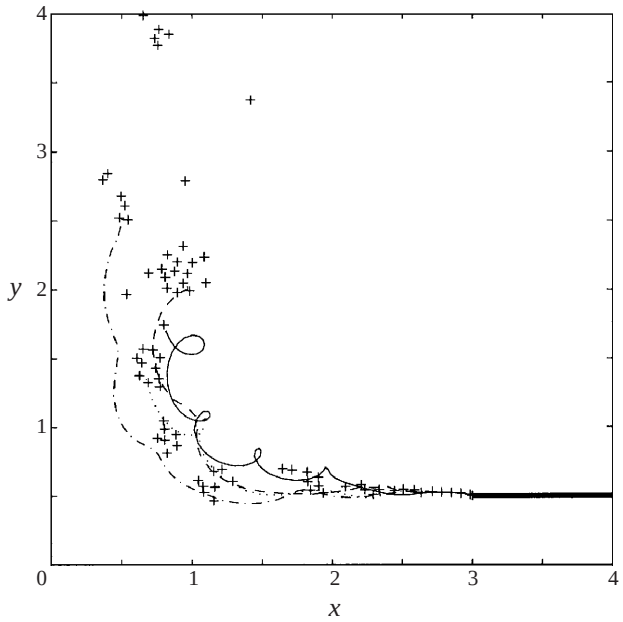

FIGURE 7. The distribution of vortex elements in the impingement region for an unforced jet at $t = 90.93$: +, vortex elements. ——, — — —, — · — and ……, traces of the vortex elements shed at $t = 81.7$, 83.1, 84.4 and 85.7 respectively.

impinging upon obstacles with sharp corners, e.g. Crighton (1992) and Rockwell & Naudascher (1979).

A similar set of the dynamic responses for the forced jet is also plotted in figure 10. At a point on the pipe exit plane, figure 10(*a*), the forcing frequency emerges from the background noise. The forced mode is slightly amplified by the instability mechanism at the two observation points near and after the impingement region, figure 10(*b*, *c*), while in the latter case, low-frequency fluctuations as well as the first subharmonic of the forcing are excited. The second subharmonic frequency eventually dominates the unsteady fluctuations of the wall jet and the forcing frequency is submerged into the background noise, figure 10(*d*).

Mean flow properties, such as the mean velocity and fluctuation intensities, are reviewed in Kuo (1998). He also uses space–time correlations of the hydraulic velocity fluctuations to estimate the convection speed of the eddies, which is around 0.6 and 0.7 of the jet exit speed. Similarities, such as the eddy speed and the onset of instabilities, are found between the two-dimensional incident jet and a cylindrical jet, see Acton (1980). Two additional time steps, $\delta t = 0.1$ and 0.2 were also investigated and both are observed to yield a similar hydraulic flow. Generally speaking, this model is capable of resolving the inner flow satisfactorily and provides a suitable basis for far-field sound calculations.

4.2. *Unforced jet*

In this section, we calculate the acoustic signals at an observation point $r_o = 3.0$. The jet is unforced. Figure 11(*a*, *b*) show the monopole $\widetilde{B}_o^{(1)}$ and the module of the quadrupole term $\widetilde{B}_o^{(21,2)}$ respectively. These terms are related to the flow motion through functions $\mathscr{P}(\Omega)$, (2.15), and $\mathscr{Q}(\Omega)$, (2.13). The contribution of the monopole is large at the initial stage. After the impingement of the starting vortex, the fluctuations

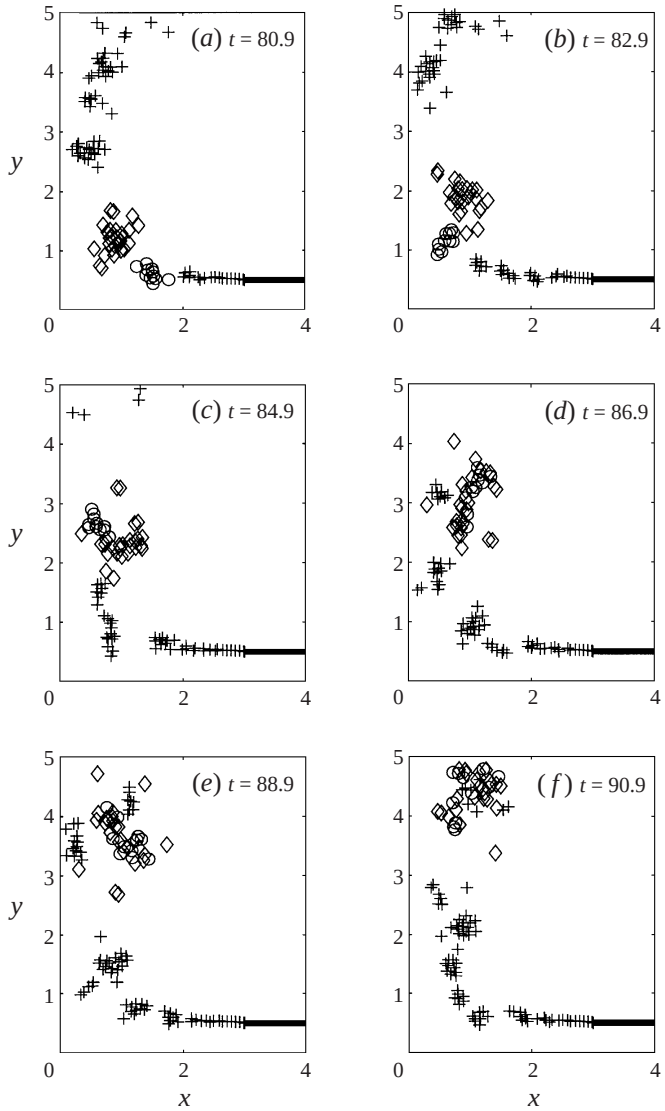

FIGURE 8. Vortex pairing in the impingement region: +, vortex elements; ◇, eddy A; ○, eddy B.

are small. Because of the growing instability in the vortex system, the motions of individual vortices become chaotic. This leads to broadband signals of fluctuations. Therefore, we concentrate only on the averaged physical quantities of the simulation, such as the root-mean-square (r.m.s.) values, in the following discussion.

The r.m.s. of the monopole is about 0.0024 in the time interval $t = 30$ to 140. The quadrupole, on the other hand, has of r.m.s. intensity of the fluctuations of about 0.28 in the same time interval. By beginning the calculation of these r.m.s. values at $t = 30$, the impingement noise of the starting vortex is excluded. The chosen time interval is valid provided the whole jet flow region remains compact. That is the case when the elapsed time $t \ll O(D/(MU))$. For low jet Mach numbers, this condition is fulfilled.

In the theoretical derivation, § 2, we find that all the monopole contributions to the

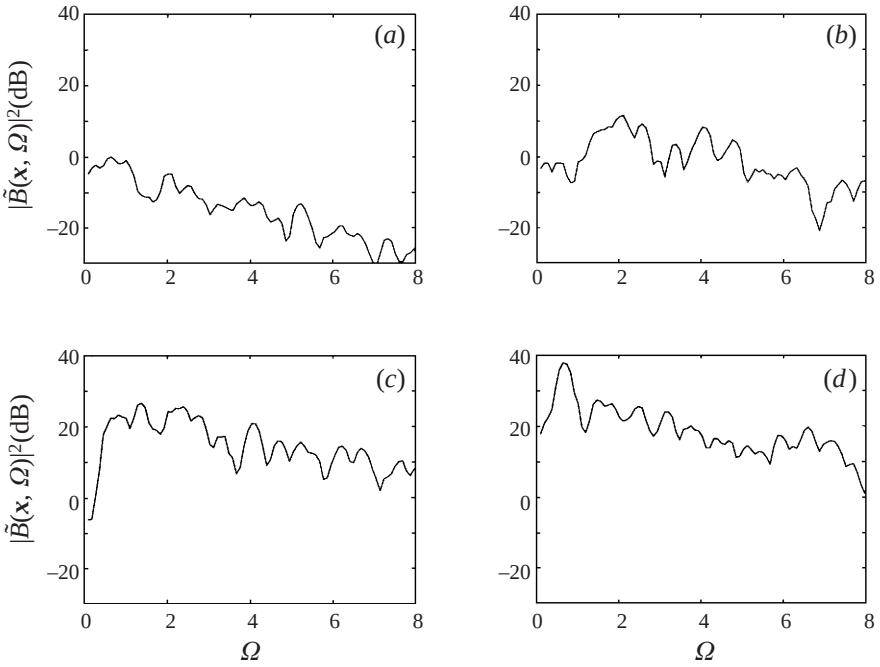

FIGURE 9. The power spectrum of the stagnation enthalpy $\tilde{B}(\boldsymbol{x}, \Omega)$ of the unforced jet against frequency Ω. (*a*) $\boldsymbol{x} = (3.0, 0)$, (*b*) $\boldsymbol{x} = (1.0, 0)$, (*c*) $\boldsymbol{x} = (0.1, 2.2)$, (*d*) $\boldsymbol{x} = (0.1, 7.0)$.

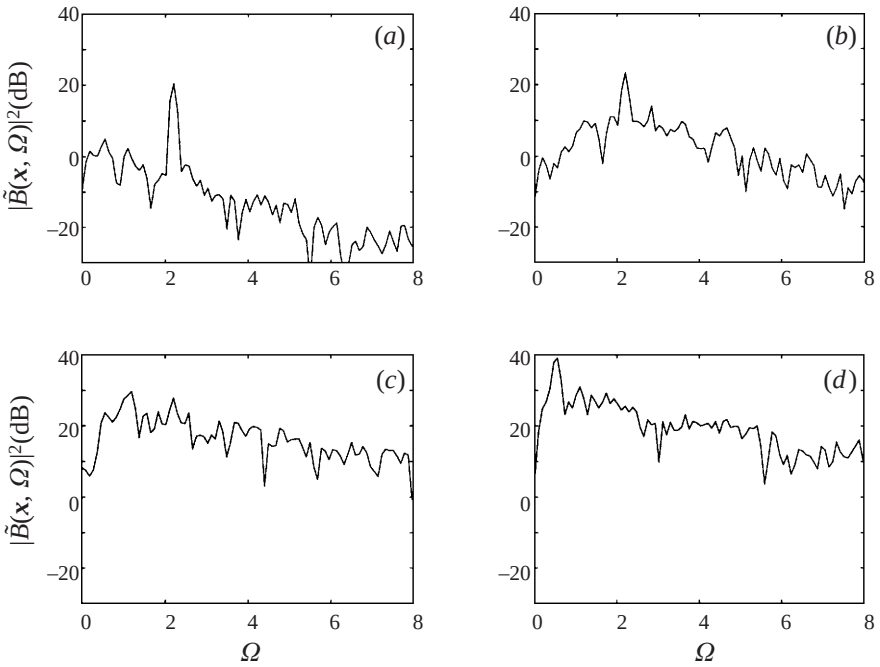

FIGURE 10. The power spectrum of the stagnation enthalpy $\tilde{B}(\boldsymbol{x}, \Omega)$ of the forced jet against frequency Ω. (*a*) $\boldsymbol{x} = (3.0, 0)$, (*b*) $\boldsymbol{x} = (1.0, 0)$, (*c*) $\boldsymbol{x} = (0.1, 2.2)$, (*d*) $\boldsymbol{x} = (0.1, 7.0)$.

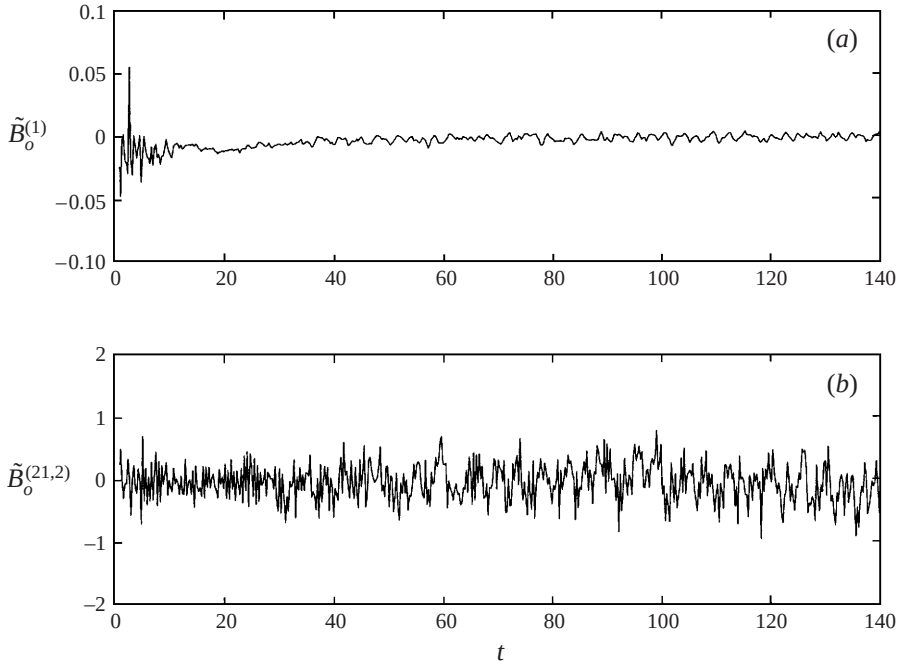

FIGURE 11. (*a*) The monopole $\tilde{B}_o^{(1)}(t, \boldsymbol{x}_o)$. (*b*) The module of the quadrupole $B_o^{(21,2)}(t, \boldsymbol{x}_o)$ at $r_o = 3.0$ for the unforced jet.

sound field are proportional to the first or second time derivative of

$$\int_{-\infty}^{t-r_o} \mathrm{d}\tau \, ((t-\tau)^2 - r_o^2)^{-1/2} \sum_i \Gamma_i \frac{\mathrm{d}}{\mathrm{d}\tau} \mathrm{Im} \left\{ \log \left(\zeta_i(\tau) + \frac{1}{a} \right) \right\}, \tag{4.1}$$

after restoring the definition of $\mathscr{P}(\Omega)$ in (2.15) and carrying out its integration over the point vortices. Γ_i and $\zeta_i(\tau)$ are the circulation and the location of individual vortex elements. $\mathrm{d}/\mathrm{d}\tau$ denotes the material derivative. The time derivative of the summation is calculated from the simulation results at successive time steps. Then, the temporal integral is carried out from the jet start to the retarded time $t - r_o$. The function $\mathrm{Im}\{\log(\zeta + 1/a)\}$ is linearly proportional to the stream function of a hypothetical potential flow with a source at infinity in the duct. Hence, this expression illustrates the mechanism of sound production: sound is generated when the vortex elements cross the hypothetical streamlines (Crighton *et al.* 1992, chap. 12). The additional integral is to sum the contribution over the third direction for the two-dimensional configuration.

From this mechanism, we expect a significant contribution when the vortex elements are near a sharp corner, such as the duct lip in the present case, where the gradient of the stream function is large in magnitude. This is seen when the jet starts. However, after the incident jet becomes fully developed, the array of representative vortex elements near the lip is only subjected to small perturbations induced by the Kelvin–Helmholtz instabilities (Rosenhead 1932 and Krasny 1987), as seen in figure 7. The change due to the motion of the existing vortex after each calculation time step is further compensated by the new vortex introduced into the flow field. Then the emerging jet no longer plays an active part in the sound generation.

The module of the quadrupole term $B_o^{(21,2)}$ has a similar sound generation mecha-

nism to that of the monopoles. For the point vortex model, $B_o^{(21,2)}$ is proportional to the second time derivative of

$$\int_{-\infty}^{t-r_o} \mathrm{d}\tau\,((t-\tau)^2 - r_o^2)^{-1/2} \sum_i \Gamma_i \frac{\mathrm{d}}{\mathrm{d}\tau} \mathrm{Im}\,\{\zeta_i(\tau)\}, \tag{4.2}$$

where $\mathrm{Im}\,\{\zeta\}$ is a hypothetic stream function with a uniform incoming flow as $y_2 \to \infty$. Its numerical implementation is similar to that of (4.1).

Since the contribution from individual vortices is weighted linearly by their location in the transformed plane, it is expected that the sum in the above expression mainly arises due to elements distant from the lip. In the time sequence in figure 11(*b*), a considerable portion of the high-frequency fluctuations first appears near the starting time. This follows the apparent short-wave instabilities of the starting vortex. As time proceeds, these high-frequency fluctuations are gradually suppressed. This may result from the merging process in the distant hydraulic field.

In a real jet, the extended wall jet eventually breaks the compactness assumption, say when $t \gtrsim O(D/(MU))$. The retarded time difference of sound emitted along the shear layer is then no longer negligible. Considering a single shear layer, Crighton & Huerre (1990) find that the acoustic field has much more fruitful characteristics when the envelope of the source is no longer compact. For example, a superdirectivity character which is not expressible in multipole terms is found if the envelope has the length scale of $1/M$. Using the method of direct numerical simulation, Colonius, Lele & Moin (1997) point out that the acoustic field predicted by the acoustic analogy is very sensitive to small changes in the description of the source in a mixing layer. These details, however, are beyond the scope of the present discussion and we shall bear in mind that the compact assumption may only be sustained for some finite time.

4.3. *Forced jet*

We now go on to calculate the sound of a forced jet. The forcing of a small velocity fluctuation far upstream in the duct is converted into a condition on stagnation enthalpy by (2.2) and noting that there is no vorticity in the duct. In non-dimensional form, this is

$$M \frac{\partial}{\partial x_D} \widetilde{B}_D(t, x_D)\Big|_{x_D \to 0} = -\frac{\partial}{\partial t} \tilde{u}' \cos(\Omega_0 t),$$

where $\widetilde{B}_D(t, x_D)$ is given by (2.43) and x_D is the duct variable. This leads to the estimation of the stagnation enthalpy magnitude of the incident sound

$$M\,B_I \simeq -\tilde{u}'/2.$$

This is roughly equal to a total stagnation enthalpy fluctuation of amplitude $\tilde{u}'/M$. The leading scattering term of the forcing, see (2.46), has an estimated root-mean-square magnitude

$$\left\langle \left| \frac{4}{\pi} M \frac{\partial \widehat{B}_I}{\partial t} \right|^2 \right\rangle^{1/2} \simeq \Omega_0 \tilde{u}'/(\pi\sqrt{r_o}). \tag{4.3}$$

As an illustrative example, the velocity fluctuation is assumed harmonic with frequency $\Omega_0 = 2.2$ and amplitude $\tilde{u}' = 0.014$. The intensity of the leading scattering, (4.3), is about 0.0057. Figure 12 shows the numerical results for the monopole terms, $\widetilde{B}_o^{(1)}$, $\widetilde{B}_o^{(22)}$ and $\widetilde{B}_o^{(21,1)}$, of the shear layer sound, (2.42). Harmonic dependence on the forcing is found in all the representative functions. The r.m.s. intensity of $\widetilde{B}_o^{(1)}$ between $t = 30$ and 140 is 0.0045. This is produced by the excited hydrodynamic fluctuations in

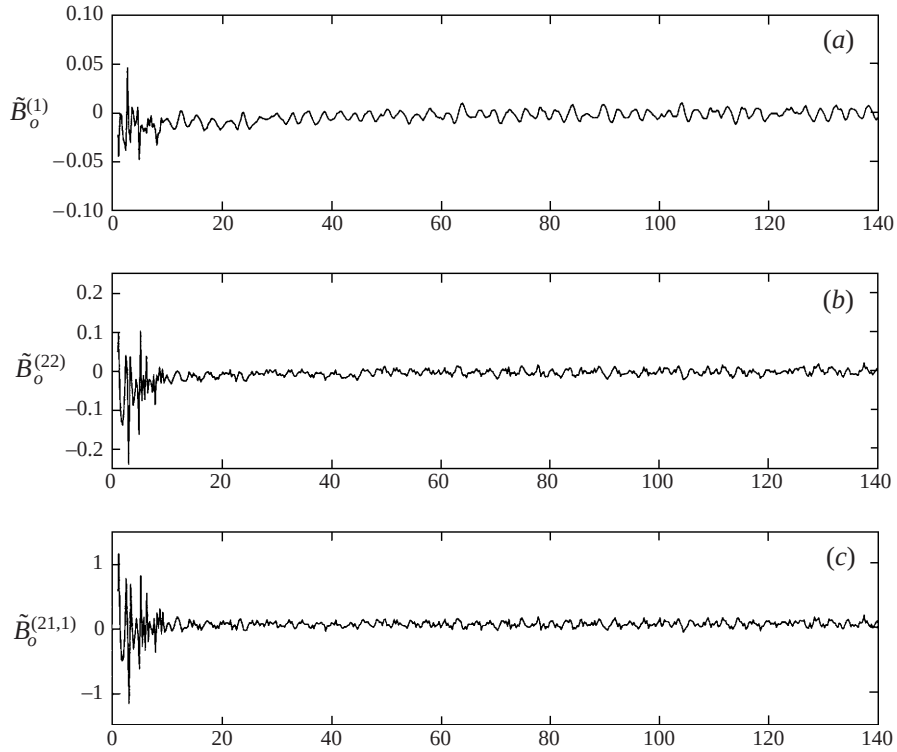

FIGURE 12. The monopoles at $r_o = 3.0$: (*a*) $\widetilde{B}_o^{(1)}(t, \boldsymbol{x}_o)$, (*b*) $\widetilde{B}_o^{(22)}(t, \boldsymbol{x}_o)$ and (*c*) $\widetilde{B}_o^{(21,1)}(t, \boldsymbol{x}_o)$ for the forced jet.

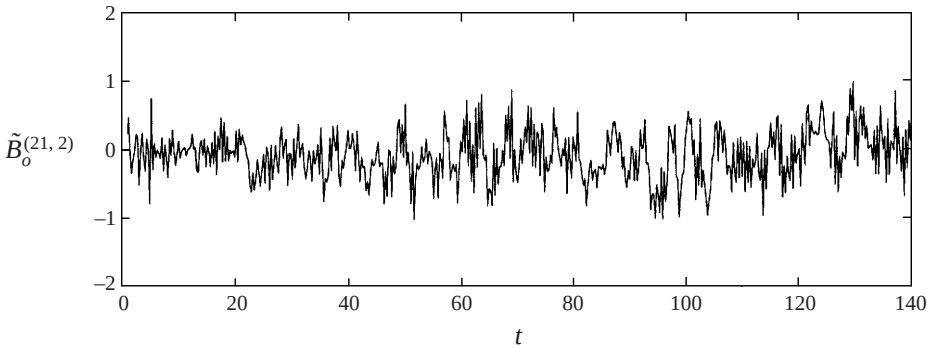

FIGURE 13. The module of the quadrupole $\widetilde{B}_o^{(21,2)}(t, \boldsymbol{x}_o)$ at $r_o = 3.0$ for the forced jet. The directivity factor is suppressed.

the jet shear layer due to the interaction of the Kutta condition and the incident wave. The r.m.s. intensity of $\widetilde{B}_o^{(22)}$ and $\widetilde{B}_o^{(21,1)}$ is 0.0072 and 0.041 respectively. Since these terms are further multiplied by small functions of jet Mach number, they do not make a significant contribution to the far-field acoustics. The intensity of the quadrupole module, figure 13, is about 0.34 and its spectrum remains broadband. This is because the quadrupole depends on the global motion of vortices in the impingement region rather than, like the monopoles, on the localized contribution near the duct exit.

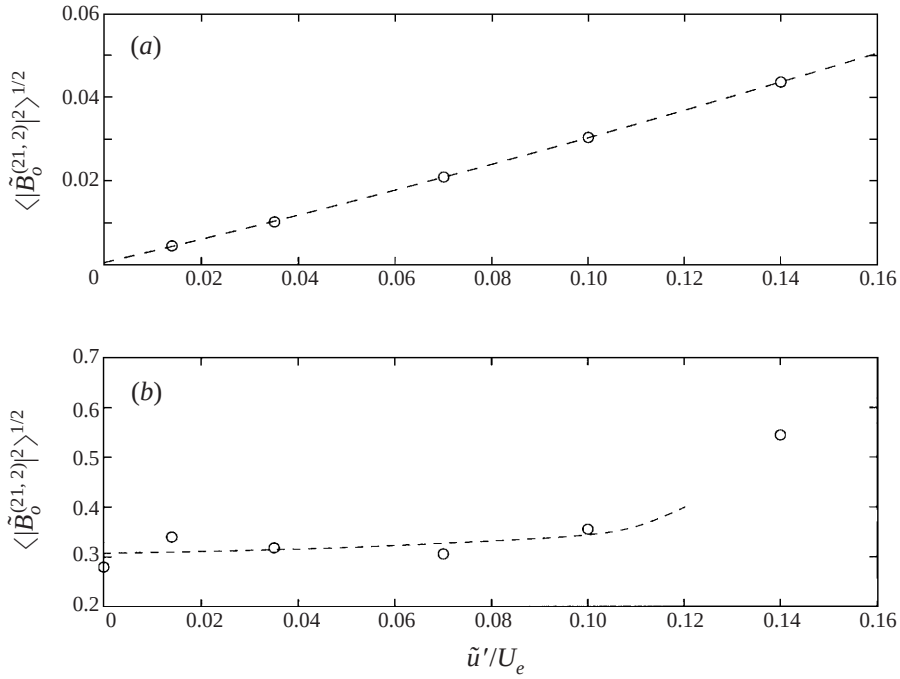

FIGURE 14. Dependence of root-mean-square intensity on the forcing magnitude at $r_o = 3.0$. (*a*) $\langle|\widetilde{B}_o^{(1)}|^2\rangle^{1/2}$, (*b*) $\langle|B_o^{(21,2)}|^2\rangle^{1/2}$.

Fixing the time step and the forcing frequency, we investigate the relationship between the forcing magnitude and the monopole $\widetilde{B}_o^{(1)}$ as well as the quadrupole module $\widetilde{B}_o^{(21,2)}$. Figure 14(*a*) shows the monopole $\widetilde{B}_o^{(1)}$ due to the flow motion and our checks have shown that it is almost independent of the time step length. The amplitude is proportional to the forcing. This linear relationship is also found for the continuous shear layer of a free jet, Howe (1979). This induced fluctuation is proportional to the product of the forcing amplitude and its frequency. He further points out that as far as the interaction with the nozzle is concerned, whether the exterior flow is stable is quite irrelevant. This is because the principal interaction between the shear layer and the nozzle occurs in a short hydrodynamic length scale. On the other hand, when the forcing $\tilde{u}'/U_e < 0.1$, the quadrupole module, figure 14(*b*) is rather insensitive and remains around 0.3. This may be due to the saturation of the nonlinear interactions between the disturbances and the impingement.

Referring to the multipole expansion of the far-field acoustics (2.46) together with (4.3) and the representative terms in figure 14, we find that the scattering term (4.3) makes the major contribution to the leading monopole when M is small. Within the current forcing level ($\tilde{u}'/U_e < 0.16$), it is less than 0.06 at the observation point. The quadrupole intensity is about $0.3M^2$. In the very low-Mach-number limit, such as a water jet, the leading monopole can be the dominant source of sound though it is weak. On the other hand, since the intensity level of the quadrupole has a larger coefficient and increases more rapidly as the square of the jet Mach number than the weak leading monopole, the quadrupole term may reach the magnitude of the monopole at reasonable Mach numbers. For example, we can estimate that, at the maximum forcing level of this calculation, the quadrupole will have a magnitude as large as the leading monopole when the jet Mach number is at least $(0.06/0.3)^{1/2} \simeq 0.45$.

5. Conclusion

The sound generation mechanism of a two-dimensional low-Mach-number impinging jet is considered. The effects of the jet pipe are included. A multipole expression for both forced and unforced cases is derived by the method of matched asymptotic expansions. For simplicity, the jet is assumed symmetric with respect to its centreline. Symmetric perturbations are observed as the primary modes when the jet speed is high enough to establish a self-sustained feedback loop, e.g. Neuwerth (1974) and Powell (1988). They are also shown to have a lower frequency band than the intrinsic properties of the free jet without the impingement plate (Tam & Ahuja 1990, Tam & Norum 1992). Nevertheless, as discussed in § 2.1, it is possible to include the asymmetric modes of the jet by applying a more sophisticated transformation with some extra algebra.

Matching processes are carried out for higher-order terms to obtain the quadrupole sound in addition to the leading monopole. Stagnation enthalpy is used as the independent variable for the acoustic waves and is normalized on the jet exit velocity. The sound source mechanism is divided into two categories. One is due to the scattering of the forcing at the nozzle exit and the other is due to the motion of the vortical shear layer. For the forced jet, the incoming waves propagating down the jet generate monopole radiation of order M, $M \log M$ and M^2.

The expression for the acoustics due to the motion of vortical shear layer has the same form for both forced and unforced cases. The leading term $\widetilde{B}_o^{(1)}$ of $O(M)$, (2.42), is a monopole resulting from the interaction between the exterior flow and the nozzle. This differs from the leading expansion of a free jet from a nozzle which is a monopole–dipole combination, Howe (1979). This is as expected, because the monopole source is reinforced by its image in the impingement surface, while the dipole is cancelled. When the forcing is not zero, the incoming sound not only induces a scattered field due to the duct exit region but also produces incompressible vortex waves through the shedding process, as described by the Kutta condition. These vortices are convected with the shear layer and are sources of sound which contribute to the far-field acoustics. Without an impingement surface, the resultant sound, as demonstrated by Howe (1979), is linearly related to the forced vortex shedding and does not depend critically on the detailed modelling of the shear flow. The accompanying monopoles of $O(M^2 \log M)$ arise from the two-dimensional configuration.

Compressibility of the primary hydraulic flow induces a monopole, or isotropic quadrupole, of the second order $O(M^2)$. The quadrupole impingement noise is also of $O(M^2)$. It has the familiar directivity pattern, with the minimum pressure fluctuations at 45° to the jet axis. The fixed pattern is imposed by the rigid boundary condition of the plate and the duct. It has the same order of magnitude as the quadrupole source of compact vortical flow in an unbounded field (Crow 1970; Möhring 1979), However, it is not the only source term and is subjected to interference from the other terms due to the presence of the nozzle pipe. This explains why the directivity pattern of the impingement quadrupole was not verified experimentally for a low-Mach-number jet until more sophisticated correlation techniques were employed (Shen & Meecham 1993).

To give numerical examples of the far-field acoustics, a point vortex model is applied to simulate the inner flow motion of impinging jets. We only investigate the symmetrical fluctuations for simplicity. A complex conformal transformation is applied to map the physical domain onto the upper half of the complex computational plane. We use the Kutta condition, which requires the finiteness of the velocity at the nozzle exit, to calculate the strength of the shed vortex at each time step. The position of the shed vortex is determined by the requirement of a 'sound-free' shedding process.

This is to prevent the generation of spurious sound due to the discretization of a continuous shear layer.

In the calculation, the monopoles, in both the forced and unforced cases, make a significant contribution when the jet starts. After the incident jet is fully developed, they are no longer as active as sources of sound. If the jet is unforced, the monopole fluctuation is induced from the instabilities of the vortex array. The intensity of the leading monopole $\widetilde{B}_o^{(1)}$ in a chosen finite time interval, § 4, is about 0.0024 at the observation point $r_o = 3.0$. Equation (4.1) implies that the magnitude of the monopoles is inversely proportional to the square root of distance to the observation point. Therefore, we have a dimensional pressure fluctuation for large r_o, of approximately $p'_{rms} \simeq 0.0024(3.0/r_o)^{1/2}M^3\rho c^2$, where ρ and c are the density and the speed of sound in the radiation field.

When the jet is forced, the incoming waves from the duct are scattered at the nozzle exit and this scattering term, $(4/\pi)M\partial\widehat{B}_I/\partial t$ in (2.46), is the major contribution to the leading monopole. The intensity of this term as a linear function of the prescribed velocity fluctuation is given by (4.3) which has a range of pressure fluctuation p'_{rms} from 0 to $0.06(3.0/r_o)^{1/2}M^2\rho c^2$ in a dimensional form for $\tilde{u}'/U_e < 0.16$. The incident waves also induce circulation fluctuations of the vortex array through the Kutta condition. They generate additional acoustic monopoles in $\widetilde{B}_o(t, \boldsymbol{x}_o)$ on the right-hand side of (2.46) after interacting with the duct pipe. This term, the same as for the corresponding free jet, is linearly dependent on the forcing level.

The quadrupole term is a Mach-number-order higher than the leading monopole. However, it has a larger coefficient. Typically, for small forcing levels, $\tilde{u}'/U_e < 0.1$, the module function $B_o^{21,2}$ is about a constant level 0.3 at the observation point $r_o = 3.0$. This magnitude, from (4.2), is also inversely proportional to r_o and the quadrupole has a directivity pattern $\cos 2\theta$ where θ is measured from the plate. This leads to a dimensional pressure fluctuation $p'_{rms} = 0.3(3.0/r_o)^{1/2}M^4\rho c^2 \cos 2\theta$. For the compact jet, the quadrupole includes the sound sources in the impingement region as well as the wall jet. The independence from the forcing level is due to the saturation of the nonlinear vortical motion in these sound source regions. Since the magnitude of this quadrupole term increases more rapidly with Mach number than the weak leading monopole, the quadrupole can become a dominant source of sound at reasonable Mach numbers. At the maximum forcing level investigated, $\tilde{u}'/U_e = 0.16$, the present calculation extrapolates to show that the quadrupole sound exceeds that from the leading monopole at Mach numbers above about 0.45.

This work was carried out while one of the author (C.-Y. K.) was in receipt of an ORS award from the Committee of Vice-Chancellors and Principals.

Appendix A. Inverse Fourier transformation of the multipole expansion

A.1. *Inverse of the monopoles of $O(M)$ and $O(M^2 \log M)$*

The inverse Fourier transformation of the monopole $B_o^{(1)}$ of $O(M)$ is

$$\mathscr{F}^{-1}\left\{-\frac{\mathrm{i}\Omega^2}{\pi}\mathscr{P}(\Omega)\mathrm{H}_0^{(1)}(\Omega r_o)\right\} = -\frac{1}{2\pi}\int_{-\infty}^{\infty}\mathrm{d}\Omega\,\frac{\mathrm{i}\Omega^2}{\pi}\mathscr{P}(\Omega)\mathrm{H}_0^{(1)}(\Omega r_o)\mathrm{e}^{-\mathrm{i}\Omega t}. \qquad (\mathrm{A}\,1)$$

Recalling the definition of $\mathscr{P}(\Omega)$, (2.15), the right-hand side of the above equation can be rewritten as

$$-\frac{1}{2\pi}\int_{-\infty}^{\infty}\mathrm{d}\Omega\int_{-\infty}^{\infty}\mathrm{d}\tau\,\frac{\mathrm{i}\Omega^2}{\pi}\widetilde{\mathscr{P}}(\tau)\mathrm{H}_0^{(1)}(\Omega r_o)\mathrm{e}^{-\mathrm{i}\Omega(t-\tau)},$$

which is equivalent to

$$\frac{\mathrm{i}}{2\pi^2}\frac{\partial^2}{\partial t^2}\int_{-\infty}^{\infty}\mathrm{d}\tau\,\widetilde{\mathscr{P}}(\tau)\int_{-\infty}^{\infty}\mathrm{d}\Omega\,\mathrm{H}_0^{(1)}(\Omega r_o)\mathrm{e}^{-\mathrm{i}\Omega(t-\tau)}. \tag{A 2}$$

Applying $\mathrm{H}_0^{(1)}(-\Omega r_o)=-\mathrm{H}_0^{(2)}(\Omega r_o)$, the inner integral is

$$\begin{aligned}\int_{-\infty}^{\infty}\mathrm{d}\Omega\mathrm{H}_0^{(1)}(\Omega r_o)\mathrm{e}^{-\mathrm{i}\Omega(t-\tau)} &= \int_0^{\infty}\mathrm{d}\Omega(\mathrm{H}_0^{(1)}(\Omega r_o)\mathrm{e}^{-\mathrm{i}\Omega(t-\tau)}-\mathrm{H}_0^{(2)}(\Omega r_o)\mathrm{e}^{\mathrm{i}\Omega(t-\tau)})\\ &= -2\mathrm{i}\int_0^{\infty}\mathrm{d}\Omega(\mathrm{J}_0(\Omega r_o)\sin\Omega(t-\tau)-\mathrm{Y}_0(\Omega r_o)\cos\Omega(t-\tau)),\end{aligned}$$

after restoring the definition of the Hankel function in terms of Bessel functions $\mathrm{J}_0(\Omega r_o)$ and $\mathrm{Y}_0(\Omega r_o)$. The last line of the equation is integrable and well tabulated, see Gradshteyn & Ryzhik (1994), so that we have

$$\int_{-\infty}^{\infty}\mathrm{d}\Omega\,\mathrm{H}_0^{(1)}(\Omega r_o)\mathrm{e}^{-\mathrm{i}\Omega(t-\tau)}=-4\mathrm{i}((t-\tau)^2-r_o^2)^{-1/2}H(t-\tau-r_o).$$

Substituting into (A 2), the inverse of the monopole is

$$\tilde{B}_o^{(1)}(t)=\frac{2}{\pi^2}\frac{\partial^2}{\partial t^2}\int_{-\infty}^{t-r_o}\mathrm{d}\tau\,((t-\tau)^2-r_o^2)^{-1/2}\widetilde{\mathscr{P}}(\tau). \tag{A 3}$$

Following the same procedures we obtain the monopole $B_o^{(22)}$ of $O(M^2\log M)$

$$\tilde{B}_o^{(22)}(t)=\frac{4}{\pi^3}\frac{\partial^3}{\partial t^3}\int_{-\infty}^{t-r_o}\mathrm{d}\tau\,((t-\tau)^2-r_o^2)^{-1/2}\widetilde{\mathscr{P}}(\tau). \tag{A 4}$$

A.2. *Inverse of the monopole of* $O(M^2)$

The monopole at this order has the complex form

$$\tilde{B}_o^{(21,1)}(t)=\mathscr{F}^{-1}\{b_o^{(21,1)}\mathrm{H}_0^{(1)}(\Omega r_o)\}=\widetilde{B}_{o1}^{(21,1)}+\widetilde{B}_{o2}^{(21,1)}+\widetilde{B}_{o3}^{(21,1)}, \tag{A 5}$$

where

$$\widetilde{B}_{o1}^{(21,1)}=\mathscr{F}^{-1}\left\{-\frac{1}{\pi}\left(\mathrm{i}\Omega^2+\frac{\Omega^3}{\pi}\mathscr{B}\right)\mathscr{P}(\Omega)\mathrm{H}_0^{(1)}(\Omega r_o)\right\},$$

$$\widetilde{B}_{o2}^{(21,1)}=\mathscr{F}^{-1}\left\{\frac{\Omega^3}{\pi^2}(\mathrm{i}\pi-2\log\Omega)\mathscr{P}(\Omega)\mathrm{H}_0^{(1)}(\Omega r_o)\right\},$$

$$\widetilde{B}_{o3}^{(21,1)}=-\mathscr{F}^{-1}\{\mathrm{i}\mathscr{R}(\Omega)\mathrm{H}_0^{(1)}(\Omega r_o)\},$$

on using $b_o^{(21,1)}$ from (2.39), (2.36) and (2.27).

Evaluating the first term is straightforward and gives

$$\widetilde{B}_{o1}^{(21,1)}=\frac{2}{\pi^2}\frac{\partial^2}{\partial t^2}\left(1+\frac{\mathscr{B}}{\pi}\frac{\partial}{\partial t}\right)\int_{-\infty}^{t-r_o}\mathrm{d}\tau\,((t-\tau)^2-r_o^2)^{-1/2}\widetilde{\mathscr{P}}(\tau). \tag{A 6}$$

To calculate $\widetilde{B}_{o2}^{(21,1)}$, we need to go through some details:

$$\widetilde{B}_{o2}^{(21,1)} = -\frac{1}{2\mathrm{i}\pi^3}\frac{\partial^3}{\partial t^3}\int_{-\infty}^{\infty}\mathrm{d}\tau\,\widetilde{\mathscr{P}}(\tau)\int_{-\infty}^{\infty}\mathrm{d}\Omega\,(2\log\Omega-\mathrm{i}\pi)\mathrm{H}_0^{(1)}(\Omega r_o)\mathrm{e}^{-\mathrm{i}\Omega(t-\tau)}$$

$$= -\frac{1}{\pi^3}\frac{\partial^3}{\partial t^3}\int_{-\infty}^{\infty}\mathrm{d}\tau\,\widetilde{\mathscr{P}}(\tau)\mathrm{Im}\left\{\int_0^{\infty}\mathrm{d}\Omega\,(2\log\Omega-\mathrm{i}\pi)\mathrm{H}_0^{(1)}(\Omega r_o)\mathrm{e}^{-\mathrm{i}\Omega(t-\tau)}\right\}, \qquad (A\,7)$$

where we use $\log(-\Omega)=\log(\Omega)+\mathrm{i}\pi$. The last integral has no exact closed form, but we can find an approximation for r_o large:

$$\mathrm{H}_0^{(1)}(\Omega r_o)\sim\sqrt{\frac{2}{\pi\Omega r_o}}\exp\left(\mathrm{i}\Omega r_o-\frac{\mathrm{i}\pi}{4}\right).$$

After substitution into (A 7), the inner integral can be carried out while the singularity at $\Omega=0$ is integrable and has negligible contribution. The approximate result is

$$\widetilde{B}_{o2}^{(21,1)}\sim\frac{2}{\pi^3}\sqrt{\frac{2}{r_o}}\frac{\partial^3}{\partial t^3}\int_{-\infty}^{t-r_o}\mathrm{d}\tau\,\widetilde{\mathscr{P}}(\tau)\frac{(\psi(1/2)-\log(t-\tau-r_o))}{(t-\tau-r_o)^{1/2}}, \qquad (A\,8)$$

where $\psi(x)$ is Euler's psi function which has value -1.96351 at $x=1/2$.

Before evaluating the third monopole, recall the definition (2.38)

$$\mathscr{R}(\Omega)=\mathscr{F}\left\{\int\left(\frac{\mathrm{D}^2}{\mathrm{D}t^2}\widetilde{B}_i^{(0)}-\frac{\mathrm{D}\boldsymbol{u}}{\mathrm{D}t}\cdot\frac{\partial\boldsymbol{u}}{\partial t}\right)\mathrm{d}\mathscr{V}_y\right\}. \qquad (A\,9)$$

Restoring the momentum equation and expanding the material time derivative, we have

$$\frac{\mathrm{D}^2}{\mathrm{D}t^2}\widetilde{B}_i^{(0)}+\frac{\mathrm{D}\boldsymbol{u}}{\mathrm{D}t}\cdot\frac{\partial\boldsymbol{u}}{\partial t}=\nabla_i\frac{p}{\rho}\cdot\frac{\partial\boldsymbol{u}}{\partial t}$$

$$+\left(\frac{\partial^2}{\partial t^2}+\frac{\partial}{\partial t}\boldsymbol{u}\cdot\nabla_i+\boldsymbol{u}\cdot\nabla_i\frac{\partial}{\partial t}+\boldsymbol{u}\cdot\nabla_i(\boldsymbol{u}\cdot\nabla_i)\right)\widetilde{B}_i^{(0)}.$$

Noting that $\nabla_i\cdot\boldsymbol{u}=0$ with only higher-order error, we can re-express the right-hand side of the above equation as

$$\frac{\partial^2}{\partial t^2}\widetilde{B}_i^{(0)}+\nabla_i\cdot\left\{\frac{p}{\rho}\frac{\partial\boldsymbol{u}}{\partial t}+\left(\frac{\partial}{\partial t}\boldsymbol{u}+\boldsymbol{u}\frac{\partial}{\partial t}+\boldsymbol{u}(\boldsymbol{u}\cdot\nabla_i)\right)\right\}\widetilde{B}_i^{(0)}. \qquad (A\,10)$$

Integrating this expression over the control volume and substituting back into (A 9), we have

$$\mathscr{F}^{-1}\{\mathscr{R}(\Omega)\}=\int\frac{\partial^2}{\partial t^2}\widetilde{B}_i^{(0)}\,\mathrm{d}\mathscr{V}_y$$

$$+\oint\mathrm{d}\mathscr{S}_y\,\boldsymbol{n}\cdot\left\{\frac{p}{\rho}\frac{\partial\boldsymbol{u}}{\partial t}+(\frac{\partial}{\partial t}\boldsymbol{u}+\boldsymbol{u}\frac{\partial}{\partial t}+\boldsymbol{u}(\boldsymbol{u}\cdot\nabla_i))\widetilde{B}_i^{(0)}\right\}, \qquad (A\,11)$$

where $\boldsymbol{n}$ is the unit vector normally outward from the boundary. The second term involves integration over the physical boundaries and a control surface at infinity. The integral over the solid boundaries vanishes because the normal velocity there is zero. Since we use discrete point vortex model to simulate the impinging jet, we have the velocity potential from (3.1). This gives a far-field velocity $\boldsymbol{u}$ which decays as $1/r_i$, and the pressure p and $B_i^{(0)}$ decay as $1/r_i^2$. Integration over the distant control surface

therefore vanishes as well. Furthermore, at infinity in the duct, the flow is steady and $\partial B_i^{(0)}/\partial x_i = 0$. The only non-zero term of (A 11) is therefore

$$\mathscr{F}^{-1}\{\mathscr{R}(\Omega)\} = \int \frac{\partial^2}{\partial t^2}\widetilde{B}_i^{(0)}\,\mathrm{d}\mathscr{V}_y - \frac{\partial}{\partial t}\widetilde{B}_i^{(0)}\bigg|_{\zeta_y\to -1/a}, \tag{A 12}$$

after integrating over the cross-section at infinity in the duct. The second term on the right-hand side $\widetilde{B}_i^{(0)}|_{\zeta_y\to -1/a}$ is $\mathscr{F}^{-1}\{\mathrm{i}\Omega\mathscr{P}(\Omega)/\pi\}$, from (2.14).

The volume integral of (A 12) is fully expanded using (2.8)

$$\int \frac{\partial^2}{\partial t^2}\widetilde{B}_i^{(0)}\,\mathrm{d}\mathscr{V}_y = \frac{\partial^2}{\partial t^2}\iint \mathrm{d}\mathscr{V}_y\,\mathrm{d}\mathscr{V}_x\,(\boldsymbol{\omega}\times\boldsymbol{u})\cdot\nabla_{ix}G(\boldsymbol{y}_i,\boldsymbol{x}_i),$$

which, using momentum equation, is equivalent to

$$-\frac{\partial^2}{\partial t^2}\iint \mathrm{d}\mathscr{V}_y\,\mathrm{d}\mathscr{V}_x\left(\frac{\partial \boldsymbol{u}}{\partial t} + \nabla_x\left(\frac{u^2}{2}+\frac{p}{\rho}\right)\right)\cdot\nabla_{ix}G(\boldsymbol{y}_i,\boldsymbol{x}_i).$$

In the present model, there is a velocity potential ϕ such that $\boldsymbol{u} = \nabla_x\phi$. Hence the above integral is

$$-\frac{\partial^2}{\partial t^2}\iint \mathrm{d}\mathscr{V}_y\,\mathrm{d}\mathscr{V}_x\,\nabla_x\left(\frac{\partial\phi}{\partial t}+\frac{u^2}{2}+\frac{p}{\rho}\right)\cdot\nabla_{ix}G(\boldsymbol{y}_i,\boldsymbol{x}_i),$$

which is zero because $\partial\phi/\partial t + u^2/2 + p/\rho$ is Bernoulli's constant for incompressible flow. Therefore, we have $\mathscr{R}(\Omega) = -\Omega^2\mathscr{P}(\Omega)/\pi$ and

$$\widetilde{B}_{o3}^{(21,1)} = -\frac{2}{\pi^2}\frac{\partial^2}{\partial t^2}\int_{-\infty}^{t-r_o}\mathrm{d}\tau\,((t-\tau)^2 - r_o^2)^{-1/2}\widetilde{\mathscr{P}}(\tau). \tag{A 13}$$

Summing over (A 6), (A 8) and (A 13), we have the monopole of $O(M^2)$

$$\tilde{B}_o^{(21,1)} = \frac{2}{\pi^3}\frac{\partial^3}{\partial t^3}\left\{\mathscr{B}\int_{-\infty}^{t-r_o}\mathrm{d}\tau\,((t-\tau)^2-r_o^2)^{-1/2}\widetilde{\mathscr{P}}(\tau)\right.$$
$$\left. +\sqrt{\frac{2}{r_o}}\int_{-\infty}^{t-r_o}\mathrm{d}\tau\,\widetilde{\mathscr{P}}(\tau)\frac{(\psi(1/2)-\log(t-\tau-r_o))}{(t-\tau-r_o)^{1/2}}\right\}, \tag{A 14}$$

where $\psi(1/2) = -1.96351$ and $\mathscr{B} = a - \log 2 - 2\log(\pi/a) + 2\gamma_E$.

A.3. *Inverse of the quadrupole*

The inverse of the quadrupole $B_o^{(21,2)}$ is

$$\mathscr{F}^{-1}\left\{\frac{\pi\Omega^3}{4}\mathscr{Q}(\Omega)\mathrm{H}_2^{(1)}(\Omega r_o)\right\} = \frac{1}{2\pi}\int_{-\infty}^{\infty}\mathrm{d}\Omega\,\frac{\pi\Omega^3}{4}\mathscr{Q}(\Omega)\mathrm{H}_2^{(1)}(\Omega r_o)\mathrm{e}^{-\mathrm{i}\Omega t}, \tag{A 15}$$

where the directivity factor has been suppressed for brevity. The Hankel function of second order is replaced by

$$\mathrm{H}_2^{(1)}(\Omega r_o) = -\frac{2}{\Omega r_o^2}\frac{\mathrm{d}}{\mathrm{d}\Omega}\mathrm{H}_0^{(1)}(\Omega r_o) - \mathrm{H}_0^{(1)}(\Omega r_o).$$

Substituting into (A 15), we have the right-hand side of the equation

$$-\frac{1}{8}\int_{-\infty}^{\infty}\mathrm{d}\Omega\,\mathscr{Q}(\Omega)\mathrm{e}^{-\mathrm{i}\Omega t}\left(\frac{2\Omega^2}{r_o^2}\frac{\mathrm{d}}{\mathrm{d}\Omega}\mathrm{H}_0^{(1)}(\Omega r_o) + \Omega^3\mathrm{H}_0^{(1)}(\Omega r_o)\right).$$

The first term decays much faster than the second. Hence, it is negligible if the observer is far away from the source region. The other term can be evaluated in a straightforward way and leads to

$$B_o^{(21,2)} = \frac{1}{2}\frac{\partial^3}{\partial t^3}\int_{-\infty}^{t-r_o} \mathrm{d}\tau\,((t-\tau)^2 - r_o^2)^{-1/2}\widetilde{\mathcal{Q}}(\tau). \tag{A 16}$$

Appendix B. Similarity solution for the departing new vortex

We have seen in § 3.2 that the equation of motion for the new vortex encounters an indefinite value just as it departs from the exit at the beginning of the time step. This is because $\Phi'(0)$ is zero at this moment. To remove this singularity, we assume that initially it moves along a straight path and that its location can be written as

$$\zeta_n = \sigma t^{\alpha}\mathrm{e}^{\mathrm{i}\theta}, \tag{B 1}$$

where σ, θ, and α are constants; t is measured relative to the beginning time of the step. In addition, $\Phi'(0)$ is presumed proportional to t, say

$$\Phi'(0) \simeq \lambda t, \tag{B 2}$$

due to the motion of the remaining vortices.

For the departing vortex, $\zeta_n \to 0$, equation (3.9) leads to

$$\alpha\sigma^2 t^{2\alpha-1}(3\mathrm{e}^{2\mathrm{i}\theta} - 1) = \frac{4\pi}{Da^2}(1+1/a)^{1/2}\lim_{\zeta_n\to 0} u(z_n) - \sigma^2 t^{2\alpha-1}(\mathrm{e}^{2\mathrm{i}\theta} - 1) \tag{B 3}$$

after substitution of (B 1) and (B 2). Bringing $\mathrm{d}\zeta_n/\mathrm{d}z_n$ and $\mathrm{d}^2\zeta_n/\mathrm{d}z_n^2$ from (2.10) into (3.3) and noting that the Kutta condition is satisfied, we find that the the finite velocity of the new vortex is

$$\lim_{\zeta_n\to 0} u(z_n) = -\frac{\sqrt{1+1/a}}{Da^2}\Big\{U_e Da^2 - \sum_j \mathrm{i}\Gamma_j\left(\frac{1}{\zeta_j^2} - \frac{1}{\zeta_j^{*2}}\right) + \frac{\mathrm{i}\Gamma_n}{\zeta_n}\left[\left(\frac{1}{\zeta_n} - \frac{1}{\zeta_n^*}\right) - \frac{1}{\zeta_n - \zeta_n^*} - \frac{1}{2\zeta_n}\right] + O(\zeta_n)\Big\}. \tag{B 4}$$

Recalling the Kutta condition (3.5) which gives the circulation Γ_n as a function of the vortex position, we have Γ_n proportional to $t^{\alpha+1}$ after incorporating (B 2). Therefore, the terms in the second line of (B 4) are proportional to $t^{1-\alpha}$ and t^{α} while those in the first line have a non-zero constant leading term.

We can then determine α by balancing the power of t of the leading terms in (B 3). This gives the only possible value of α to be $1/2$. Neglecting the small terms proportional to $t^{1-\alpha}$ on the right-hand side of (B 4), $\lim_{\zeta_n\to 0} u(z_n)$ is a real function. Therefore, we have that $\theta = \pi/2$ from (B 3). This shows that the new vortex leaves the exit tangentially to the pipe. Finally, we obtain the solution for σ

$$\sigma^2 = \frac{\pi}{D^2a^4}\left(1+\frac{1}{a}\right)\left\{U_e Da^2 - \sum_j \mathrm{i}\Gamma_j\left(\frac{1}{\zeta_j^2} - \frac{1}{\zeta_j^{*2}}\right)\right\}, \tag{B 5}$$

after putting α, θ and (B 4) into (B 3).

The indefinite value at the start of the time step is therefore removed. The constants α, θ and σ are substituted into (B 1) and give the first extrapolated location of the new vortex after a time step at $t = \delta t$.

REFERENCES

Acton, E. 1980 A modelling of large eddies in an axisymmetric jet. *J. Fluid Mech.* **98**, 1–31.

Baker, G. R. 1979 The 'cloud in cell' technique applied to the roll up of vortex sheets. *J. Comput. Phys.* **31**, 76–95.

Brown, C. E. & Michael, W. H. 1954 Effect of leading edge separation on the lift of a delta wing. *J. Aero. Sci.* **21**, 690–706.

Colonius, T., Lele, S. K. & Moin, P. 1997 Sound generation in a mixing layer. *J. Fluid Mech.* **330**, 375–409.

Crighton, D. G. 1992 The jet edge–tone feedback cycle; linear theory for the operating stages. *J. Fluid Mech.* **234**, 361–391.

Crighton, D. G., Dowling, A. P., Ffowcs Williams, J. E., Heckl, M. & Leppington, F. G. 1992 *Modern Methods in Analytical Acoustics.* Chapter 13, Springer.

Crighton, D. G. & Huerre, P. 1990 Shear layer pressure fluctuations and superdirectivity acoustic sources. *J. Fluid Mech.* **220**, 355–368.

Crow, S. C. 1970 Aerodynamic sound emission as a singular perturbation problem. *J. Acoust. Soc. Am.* **34**, 902–906.

Crow, S. C. & Champagne, F. H. 1971 Orderly structure in jet turbulence. *J. Fluid Mech.* **48**, 547–591.

Disselhorst, J. H. M. & Wijngaarden, L. van 1980 Flow in the exit of open pipes during acoustic resonance. *J. Fluid Mech.* **99**, 293–319.

Gradshteyn, I. S. & Ryzhik, I. M. 1994 *Table of Integrals, Series, and Products,* Academic.

Hildebrand, F. B. 1956 *Introduction to Numerical Analysis.* McGraw–Hill.

Ho, C. M. & Nosseir, N. S. 1981 Dynamics of an impinging jet. Part 1. The feedback phenomenon. *J. Fluid Mech.* **105**, 119–142.

Howe, M. S. 1975 Contributions to the theory of aerodynamic sound, with application to excess jet noise and the theory of the flute. *J. Fluid Mech.* **71**, 625–673.

Howe, M. S. 1979 Attenuation of sound in low Mach number nozzle flow. *J. Fluid Mech.* **91**, 209–229.

Howe, M. S. 1996 Emendation of the Brown & Michel equation, with application to sound generation by vortex motion near a half-plane. *J. Fluid Mech.* **329**, 89–101.

Knio, O. M., Collorec, L. & Juve, D. 1995 Numerical study of sound emission by 2d regular and chaotic vortex configurations. *J. Comput. Phys.* **116**, 226–246.

Kober, H. 1952 *Dictionary of Conformal Representations.* Dover.

Krasny, R. 1987 Computation of vortex sheet roll–up in the trefftz plane. *J. Fluid Mech.* **184**, 123–155.

Kuo, C. Y. 1998 The acoustics of impinging jets. PhD thesis, University of Cambridge.

Möhring, W. 1978 On vortex sound at low Mach number. *J. Fluid Mech.* **85**, 685–691.

Möhring, W. 1979 Modelling low mach number noise. In *Mechanics of Sound Generation in flows.* (ed. E. A. Muller), pp. 85–96. Springer.

Moore, D. W. 1974 A numerical study of the roll–up of a finite vortex sheet. *J. Fluid Mech.* **63**, 225–235.

Neuwerth, G. 1974 Acoustic feedback of a subsonic and supersonic free jet which impinges on an obstacle. *NASA TT* F-15719.

Obermeier, F. 1985 Aerodynamic sound generation caused by viscous processes. *J. Sound Vib.* **99**, 111–120.

Olsen, W. A., Miles, J. H. & Dorsch, R. G. 1972 Noise generated by impingement of a jet upon a large flat board. *NASA TN* D-7075.

Peters, M. C. A. M. 1993 Aeroacoustic sources in internal flows. PhD thesis, Eindhoven University of Technology.

Peters, M. C. A. M. & Hirschberg, A. 1993 Acoustically induced periodic vortex shedding at sharp edged open channel ends: simple vortex models. *J. Sound Vib.* **161**, 281–299.

Powell, A. 1988 The sound-producing oscillations of round underexpanded jets impinging on normal plates. *J. Acoust. Soc. Am.* **83**, 515–533.

Powell, A. 1991 Nature of the sound sources in low–speed jet impingement. *J. Acoust. Soc. Am.* **90**, 3326–3331.

Rockwell, D. & Naudascher, E. 1979 Self-sustained oscillations of impinging free shear layers. *Ann. Rev. Fluid Mech.* **11**, 67–94.

Rosenhead, L. 1932 The formation of vortices from a surface discontinuity. *Proc. R. Soc. Lond.* A **134**, 170–192.

Shen, J. & Meecham, C. 1993 Quadrupole directivity of jet noise when impinging on a large rigid plate. *J. Acoust. Soc. Am.* **94**, 1415–1424.

Sutherland, L. C. & Brown, D. 1972 Prediction methods for near field noise environments of vtol aircraft. *AFFDL–TR*–71–180, Air Force Flight Dynamics Laboratory, Wright–Patterson Air Force Base, Ohio.

Tam, C. K. W. & Ahuja, K. K. 1990 Theoretical model of discrete tone generation by impinging jets. *J. Fluid Mech.* **214**, 67–87.

Tam, C. K. W. & Norum, T. D. 1992 Impingement tones of large aspect ratio supersonic rectangular jets. *AIAA* J. **30**, 304–311.

Yates, J. E. 1978 Application of the Bernoulli enthalpy concept to the study of vortex noise and jet impingement noise. *NASA CR* 2987.